Improved models for the near-Earth asteroids (2100) Ra-Shalom, (3103) Eger, (12711) Tukmit, and (161989) Cacus

Javier Rodríguez Rodríguez [1]*, E. Díez Alonso [1,2]*, Santiago Iglesias Álvarez [1],
Saúl Pérez Fernández [1], Javier Licandro [3,4]*, Miguel R. Alarcon [3,4], Miquel Serra-Ricart,[3,4]
Noemi Pinilla-Alonso [5], Susana del Carmen Fernández [1] and Francisco Javier de Cos Juez [1,6]

[1]*Instituto Universitario de Ciencias y Tecnologías Espaciales de Asturias (ICTEA), University of Oviedo, C. Independencia 13, E-33004 Oviedo, Spain*
[2]*Departamento de Matemáticas, Facultad de Ciencias, Universidad de Oviedo, E-33007 Oviedo, Spain*
[3]*Instituto de Astrofísica de Canarias (IAC), C/Vía Láctea sn, E-38205 La Laguna, Spain*
[4]*Departamento de Astrofísica, Universidad de La Laguna, E-38206 La Laguna, Tenerife, Spain*
[5]*Florida Space Institute, University of Central Florida, Orlando, FL 32816, USA*
[6]*Departamento de Explotación y Prospección de Minas, Universidad de Oviedo, E-33004 Oviedo, Spain*

ABSTRACT
We present 24 new dense light curves of the near-Earth asteroids (3103) Eger, (161989) Cacus, (2100) Ra-Shalom, and (12711) Tukmit, obtained with the Instituto Astrofísico Canarias 80 and Telescopio Abierto Remoto 2 telescopes at the Teide Observatory (Tenerife, Spain) during 2021 and 2022, in the framework of projects visible NEAs observations survey and NEO Rapid Observation, Characterization and Key Simulations. The shape models and rotation state parameters (P, λ, β) were computed by applying the light curve inversion method to the new data altogether with the archival data. For (3013) Eger and (161989) Cacus, our shape models and rotation state parameters agree with previous works, though they have smaller uncertainties. For (2100) Ra-Shalom, our results also agree with previous studies. Still, we find that a Yarkovsky–O'Keefe–Radzievskii–Paddack acceleration of $\upsilon = (0.223 \pm 0.237) \times 10^{-8}$ rad d^{-2} slightly improves the fit of the light curves, suggesting that (2100) Ra-Shalom could be affected by this acceleration. We also present for the first time a shape model for (12711) Tukmit, along with its rotation state parameters ($P = 3.484900 \pm 0.000031$ h, $\lambda = 27° \pm 8°$, $\beta = 9° \pm 15°$).

Key words: techniques: photometric – minor planets, asteroids: general – minor planets, asteroids: individual: Ra-Shalom – minor planets, asteroids: individual: Eger – minor planets, asteroids: individual: Tukmit – minor planets, asteroids: individual: Cacus.

1 INTRODUCTION

An asteroid is classified as a near-Earth asteroid (NEA) if it reaches its perihelion at a distance of less than 1.3 astronomical units (au) from the Sun as stated in Center for Near Earth Object Studies (CNEOS)[1]. Therefore, NEAs are the subgroup of minor bodies that come closest to the Earth. According to CNEOS,[2] as of 04/24/2023, there are 31 756 confirmed NEAs, of which 10 398 have a typical size greater than 140 m and 851 are larger than 1 km (the largest confirmed to date is (1036) Ganymed, with a diameter of ∼41 km, while the smaller known NEAs, as 2015 TC25, have radii of ∼1 m).

Among all the objects in this group, there is a subgroup known as Potentially Hazardous Asteroids (PHAs), which according to CNEOS[13] are those that represent a potential risk of collision with the Earth. More specifically, an asteroid is classified as PHA if its orbit has a Minimum Orbit Intersection Distance (MOID) with the Earth of 0.05 au or less and its absolute magnitude is $H < 22$, which implies that the object is larger than ∼140 m. These objects are fundamental due to their proximity to the Earth and the possibility of a collision. By monitoring and studying these asteroids, we can accurately characterize and make them a potential resource source if their composition is rich in any interesting element. From the asteroids presented in this work, (161989) Cacus belongs to this group since its MOID is 0.014085 au and its H is 17.2 from data of European Space Agency (ESA) Near Earth Objects Coordination Centre (NEOCC).[4]

To obtain the models, it's widely applied the Convex Inversion Method detailed in Kaasalainen & Torppa (2001), Kaasalainen, Torppa & Muinonen (2001), which generates a convex model and its corresponding spin state from a suitable set of light curves. In the process, both the spin state and the shape are fitted at the same

*E-mail: rodriguezrjavier@uniovi.es (JRR); diezenrique@uniovi.es (EDA); jlicandr@iac.es (JL)

[1]https://cneos.jpl.nasa.gov/about/neo_groups.html
[2]https://cneos.jpl.nasa.gov/stats/totals.html
[3]https://cneos.jpl.nasa.gov/glossary/PHA.html

[4]https://neo.ssa.esa.int/search-for-asteroids?tab=summary&des = 161989%20Cacus

time, searching for the set of parameters (complete spin state and the corresponding shape) that best reproduce the observed light curves of the asteroid. The light curves can be *dense* (that is, observations made at high cadence, of the order of minutes, and typically spanning a few hours) or *sparse* (a few observations per night but typically extending for years). Dense light curves are usually the result of specific follow-up programs, such as the Visible NEAs Observations Survey (ViNOS; Licandro et al. (2023)), while sparse light curves are usually obtained from surveys that periodically patrol the sky, such as the Asteroid Terrestrial-impact Last Alert System (ATLAS; Heinze et al. (2018), Tonry et al. (2018)), the All-Sky Automated Survey for Supernovae (ASAS-SN; Kochanek et al. (2017)), or the Wide Angle Search for Planets (SuperWASP; Parley et al. (2005)) among many others. In the light curve inversion process, it's possible to work only with dense data (Torppa et al. 2003; Ďurech et al. 2007), only sparse data (Ďurech et al. 2016; Ďurech, Hanuš & Vančo 2019), or a well-balanced combination of both (Ďurech et al. 2009b). However, to obtain reliable results, the light curves must be acquired by covering the widest possible range of phase angles, which results in observations corresponding to different geometries that encode information related to the main features of the asteroids. A large number of asteroid models, along with their parameters, light curves and many other products, is available at the Database of Asteroid Models from Inversion Techniques (DAMIT[5]; Ďurech, Sidorin & Kaasalainen (2010)), operated by The Astronomical Institute of the Charles University (Prague, Czech Republic).

Small asteroids make up the vast majority of the NEA population (97.3 per cent is estimated to have a diameter smaller than 1 km, according to CNEOS[2]). Two critical mechanisms acting on these small bodies are the Yarkovsky (Yarkovsky 1901; Bottke et al. 2006; Vokrouhlický et al. 2015) and the Yarkovsky–O'Keefe–Radzievskii–Paddack (YORP; Yarkovsky (1901), Radzievskii (1952), Paddack (1969), O'Keefe (1976), Bottke et al. (2006), Vokrouhlický et al. (2015)) effects. The first consists of orbital changes due to thermal reemission of the absorbed solar radiation, increasing the orbit's semimajor axis if the asteroid is a prograde rotator and decreasing it otherwise. It also plays a crucial role in injecting new NEAs from the Main Asteroid Belt (Chesley et al. 2003; Morbidelli & Vokrouhlický 2003). The YORP effect is a constant change in the spin state caused by anisotropic thermal re-emission and the resulting torque.

There are several observations attributed to the YORP effect that are considered as indirect detections. One is the clustering in the directions of the rotation axes among members of the same asteroid family; for example, this clustering has been observed among the Koronis members (Slivan 2002). It is also thought to be responsible of the bimodalities observed in the rotation rates (Pravec et al. 2008) and obliquities (Hanuš et al. 2013b) for small asteroids. Furthermore, it is believed to be a prominent mechanism in the formation of small binaries (Walsh, Richardson & Michel 2008).

The first direct detection of the YORP effect was in the NEA (6489) Golevka utilizing radar techniques (Chesley et al. 2003). Later it has also been detected from photometric data in (1862) Apollo (Kaasalainen et al. 2007), (54509) 2000 PH5 (Lowry et al. 2007; Taylor et al. 2007), (1620) Geographos (Ďurech et al. 2008), (25143) Itokawa, (Lowry et al. 2014), (1685) Toro, (3103) Eger, and (161989) Cacus (Ďurech et al. 2018).

In Section 2 of this work, we present new dense light curves of the NEAs (2100) Ra-Shalom, (3103) Eger, (12711) Tukmit, and (161989) Cacus, acquired at Teide Observatory. In Section 3, we

explain how these observations have been processed along with archival light curves to compute the shape models and rotational state applying the light-curve inversion method. Results are presented and compared to previous published models in Section 4. Finally, our conclusions are presented in Section 5.

2 OBSERVATIONS

Time series photometry of NEAs (2100) Ra-Shalom, (3103) Eger, (12711) Tukmit, and (161989) Cacus were obtained in the framework of ViNOS (Licandro et al. 2023), aimed to characterize NEAs by using spectroscopic, spectrophotometric, and light-curve observations, and the NEO Rapid Observation, Characterization, and Key Simulations (NEOROCKS[6]) project, where the Instituto Astrofísico Canarias (IAC) team lead the task on the characterization of radar targets. We note that the NEAs studied in this paper were observed using radar: 2100 in Ostro et al. (1984) and Shepard et al. (2000, 2008b); 3103 in Benner et al. (1997), 12711 in Benner et al. (2008), and 161989 with Goldstone in 2022 August 24.[7]

Photometric observations were obtained using two telescopes located at Teide Observatory (TO, Tenerife, Canary Islands, Spain), the Instituto Astrofísico Canarias 80 (IAC80) and Telescopio Abierto Remoto 2 (TAR2) telescopes. The observational circumstances are shown in Table 1.

The IAC80 is a 82 cm telescope with $f/D = 11.3$ in the Cassegrain focus. It is equipped with the CAMELOT-2 camera, a back-illuminated e2v 4×4 K pixels CCD of 15 μm^2 pixels, a plate scale of 0.32 arcsec pixel^{-1}, and a field of view of 21.98×22.06 arcmin^2. We used a Sloan *r* filter. Observations were done using sidereal tracking, so the asteroid's proper motion limited the images' individual exposure time. We selected exposure times such that the asteroid trail was smaller than the typical FWHM of the IAC80 images (~1.0 arcsec). The images were bias and flat-field corrected in the standard way; there was no need to correct the dark current since it is almost 0 for these CCD, so correcting the bias is enough.

TAR2 is a 46-cm $f/D = 2.8$ robotic telescope. Until July 2022, TAR2 was equipped with a FLI-Kepler KL400 camera, since then, it has been equipped with a QHY600PRO camera. The FLI-Kepler KL400 camera has a back illuminated 2×2 K pixels GPixel GSense400 CMOS with a pixel size of 11 μm^2 that in the prime focus of TAR2 has a plate scale of 1.77 arcsec pixel^{-1} and a field of view of ~1 deg^2. The QHY600PRO camera detector is a Sony back illuminated 9×6 K pixels IMX455 CMOS of 3.76 μm^2 pixels, that in the prime focus of TAR2 has a plate scale of 0.65 arcsec pixel^{-1} and a field of view of ~1.6×1.1 deg^2. Both CMOS use a rolling shutter and have the advantage of zero dead time between images. For a complete description of the QHY600PRO capabilities, see Alarcon et al. (2023). The images were biased, dark, and flat-field corrected in the standard way. With both cameras, we obtained a continuous series of 10 s images without filter (Clear) or using a Johnson *V* filter with the FLI camera and a UV/IR cut *L*-filter with the QHY with the telescope moving in sidereal tracking. To increase the SNR, consecutive images were aligned and combined to produce a final series of images of larger exposure time. In general, the number of images used to obtain the final combined one is determined by the proper motion of the NEA. This is computed such that the total exposure time is shorter than the time it takes for the

[5] https://astro.troja.mff.cuni.cz/projects/damit/

[6] https://www.neorocks.eu/
[7] https://echo.jpl.nasa.gov/asteroids/Cacu/Cacus.2022.goldstone.planning.html

Table 1. Observational circumstances of new light curves acquired by ViNOS. The table includes the object, telescope, and filters used (*r*-sloan, *V*, Clear and Luminance), the date and the starting and end time (UT) of the observations, the phase angle (α), the heliocentric (r) and geocentric (Δ) distances, and phase angle bisector longitude (PABLon) and latitude (PABLat) of the asteroid at the time of observation.

Asteroid	Telescope	Filter	Exp. time [s]	Date	UT (start)	UT (end)	$\alpha[°]$	r [au]	Δ [au]	PABLon [°]	PABLat [°]
2100 Ra-Shalom (1978 RA)	IAC80	r	45	2022-Jul-29	00:45:17.539	5:24:43.286	68.35	1.0858	0.2885	349.56	25.5341
2100 Ra-Shalom (1978 RA)	IAC80	r	45	2022-Aug-02	00:34:00.941	5:12:47.808	64.28	1.1031	0.2725	349.861	24.4537
2100 Ra-Shalom (1978 RA)	TAR2	L	60	2022-Aug-05	01:32:32.755	5:07:01.430	60.92	1.1152	0.2602	349.888	23.6158
2100 Ra-Shalom (1978 RA)	TAR2	L	30	2022-Aug-24	20:58:08.803	0:52:10.186	30.6	1.1731	0.194	344.45	16.4497
2100 Ra-Shalom (1978 RA)	TAR2	L	30	2022-Aug-26	20:33:01.210	3:59:47.558	26.93	1.1769	0.1907	343.353	15.4405
2100 Ra-Shalom (1978 RA)	TAR2	L	30	2022-Sep-06	20:17:37.248	1:17:07.642	16.42	1.1915	0.1929	336.953	8.9531
2100 Ra-Shalom (1978 RA)	TAR2	L	30	2022-Sep-08	00:19:01.430	3:13:47.453	17.28	1.1924	0.1953	336.353	8.2298
3103 Eger (1982 BB)	TAR2	Clear	60	2021-Jul-03	00:51:30.010	4:29:21.984	51.95	1.2062	0.3806	323.062	10.7387
3103 Eger (1982 BB)	TAR2	Clear	60	2021-Jul-04	00:45:43.978	5:14:49.027	52.32	1.2007	0.3723	323.984	10.2764
3103 Eger (1982 BB)	TAR2	Clear	60	2021-Jul-05	00:46:34.003	5:14:39.005	52.71	1.1952	0.364	324.927	9.7906
3103 Eger (1982 BB)	TAR2	Clear	50	2021-Jul-17	01:46:36.019	5:18:16.992	59.39	1.1299	0.2796	337.787	1.8092
3103 Eger (1982 BB)	TAR2	Clear	50	2021-Jul-18	01:46:36.970	5:27:30.038	60.16	1.1246	0.2742	338.986	0.9327
3103 Eger (1982 BB)	TAR2	Clear	50	2021-Jul-19	01:46:46.042	5:30:09.965	60.96	1.1193	0.2691	340.204	0.0191
3103 Eger (1982 BB)	TAR2	V	90	2021-Dec-13	02:18:08.957	6:13:05.030	54.13	1.213	0.653	140.013	− 10.1599
3103 Eger (1982 BB)	TAR2	V	60	2022-Feb-12	01:54:58.954	6:55:11.021	12.56	1.5281	0.562	149.456	11.7599
3103 Eger (1982 BB)	TAR2	V	60	2022-Feb-13	01:21:01.037	6:53:21.034	12.3	1.5326	0.5656	149.371	12.022
3103 Eger (1982 BB)	TAR2	V	90	2022-Mar-01	20:04:46.992	2:10:05.030	17.04	1.6053	0.6627	148.428	15.5233
12711 Tukmit (1991 BB)	TAR2	V	90	2021-Dec-28	02:57:19.469	6:45:29.030	26.94	1.433	0.5388	123.23	7.243
12711 Tukmit (1991 BB)	TAR2	V	90	2022-Aug-04	21:00:01.037	0:05:17.261	89.3	0.9779	0.2827	333.589	58.4229
12711 Tukmit (1991 BB)	TAR2	V	60	2022-Sep-05	20:29:33.590	3:52:59.750	64.07	1.1164	0.5806	347.955	63.1137
161989 Cacus (1978 CA)	IAC80	r	20	2022-Feb-22	20:09:12.154	3:56:50.352	45.52	1.2199	0.3846	121.14	− 22.2578
161989 Cacus (1978 CA)	TAR2	L	20	2022-Aug-25	01:00:10.310	1:43:30.518	93.77	1.0022	0.0825	15.7717	29.7916
161989 Cacus (1978 CA)	TAR2	L	10	2022-Sep-04	01:30:17.885	5:38:49.229	61.49	1.0367	0.0619	12.2694	− 14.1511

Table 2. Results obtained in this work for each asteroid, we show type of model (linearly increasing period (L) and constant period (C)), rotation period, geocentric ecliptic coordinates of the spin pole (λ, β), obliquity (ϵ), and YORP acceleration (υ) if the model has linearly increasing period (L).

Asteroid	Model	Period [h]	$\lambda[°]$	$\beta[°]$	$\epsilon[°]$	υ [rad d^{-2}]
2100 Ra-Shalom (1978 RA)	C	19.820056 ± 0.000012	278 ± 18	-60 ± 8	162 ± 10	–
2100 Ra-Shalom (1978 RA)	L	19.820107 ± 0.000040	278 ± 8	-60 ± 5	165 ± 5	$(0.22 \pm 0.16) \times 10^{-8}$
3103 Eger (1982 BB)	L	5.710148 ± 0.000006	214 ± 3	-71 ± 1	177 ± 1	$(0.85 \pm 0.05) \times 10^{-8}$
12711 Tukmit (1991 BB)	C	3.484900 ± 0.000031	27 ± 8	9 ± 15	119 ± 15	–
161989 Cacus (1978 CA)	L	3.755067 ± 0.000001	251 ± 6	-62 ± 2	177 ± 2	$(1.91 \pm 0.05) \times 10^{-8}$
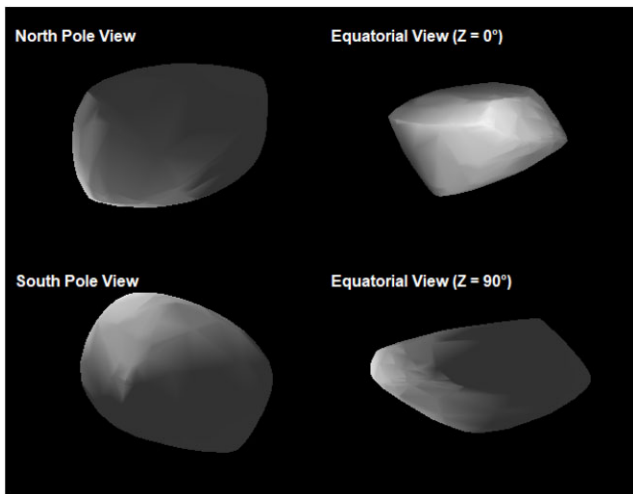
Figure 1. Constant rotation period shape model of (2100) Ra-Shalom. Left top: North Pole View (*Y*-axis = 0°). Left bottom: South Pole View (*Y*-axis = 180°). Right top and bottom: Equatorial Views with *Z*-axis rotated 0° and 90°.
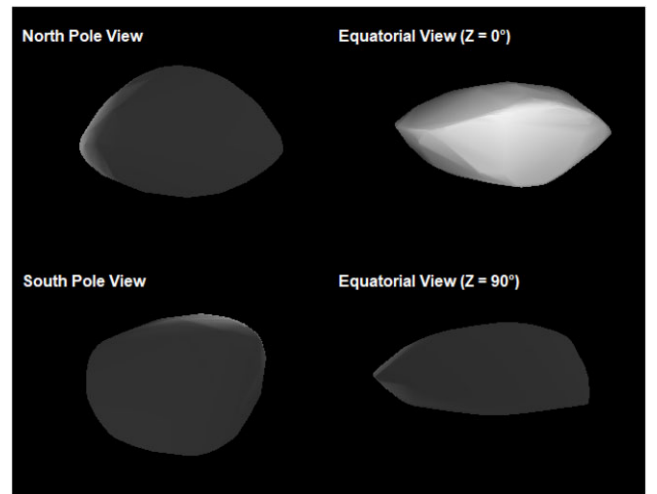
Figure 2. Linearly increasing rotation period shape model of (2100) Ra-Shalom. Left top: North Pole View (*Y*-axis = 0°). Left bottom: South Pole View (*Y*-axis = 180°). Right top and bottom: Equatorial views with *Z*-axis rotated 0° and 90°.
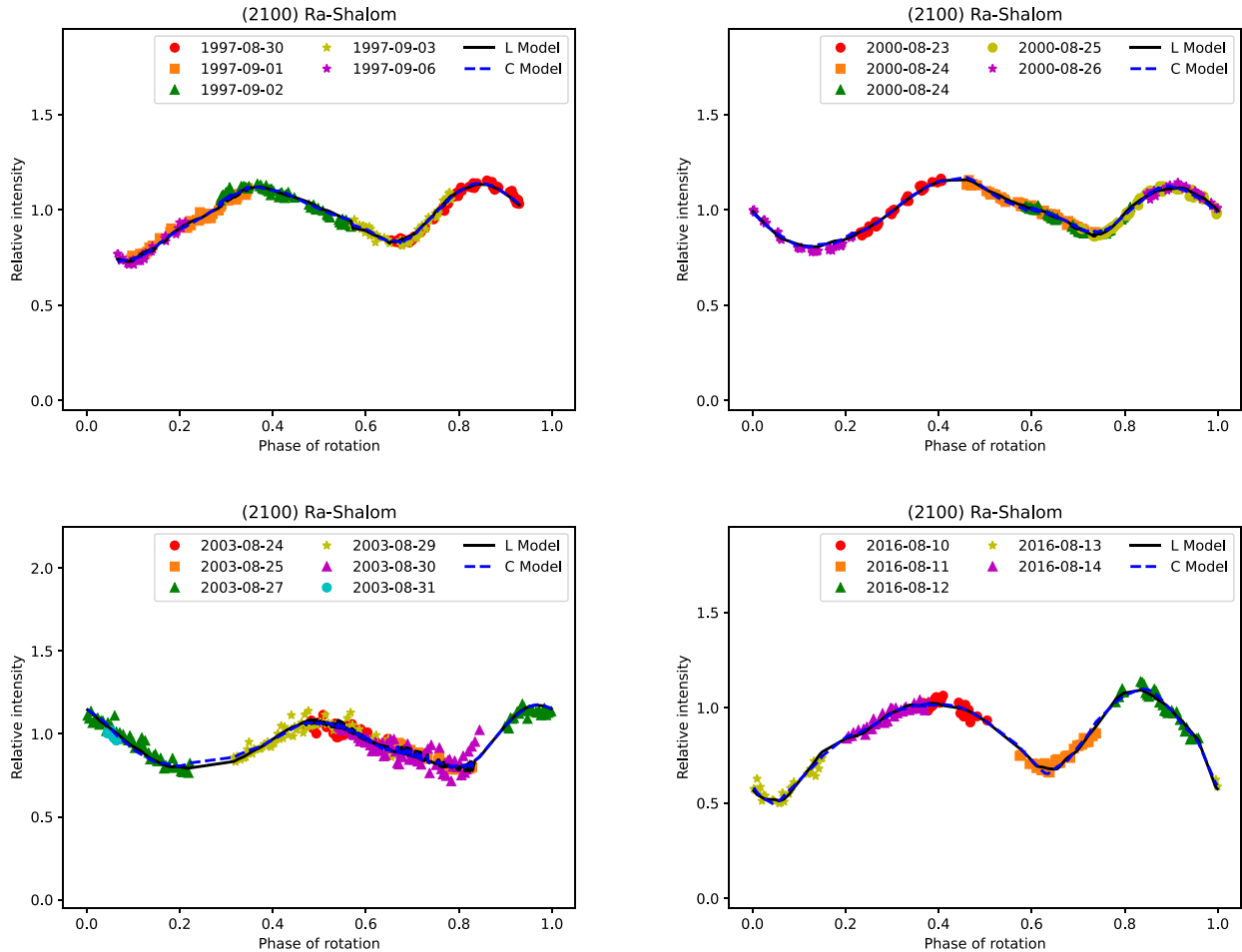
Figure 3. Fits between sets of light curves of (2100) Ra-Shalom corresponding to the 1997, 2000, 2003, and 2016 seasons and the best-fitting models. Dashed blue: best constant period model (C Model). Solid black: best linearly increasing period model (L Model). Data for each observation represented by the colour and shapes shown in each legend.

asteroid trail to be equal to the typical FWHM of this telescope (∼3.6 arcsec).

To obtain the light curves, we did aperture photometry of the final images using the Photometry Pipeline[8] (PP) software (Mommert 2017), as we did in (Licandro et al. 2023). The images obtained with the *L*-filter were calibrated to the *r* SLOAN band using the Pan-STARRS catalogue, while the other images were calibrated to the corresponding bands for the filters used.

The new light curves are presented in Appendix C along with the synthetic models computed following the method explained in Section 3 (see Figs C1 for (2100) Ra-Shalom, C2 for (3103) Eger, C3 for (161989) Cacus, and Fig. 10 in Section 4.3 for (12711) Tukmit).

3 METHODS

When discussing asteroid characterization, some basic parameters are needed to create the asteroid's model, which we will further describe next. First of all, the sidereal rotation period (*P*) is the time the asteroid takes to complete a single revolution over its rotation axis and adopt the background stars as the reference frame. It is derived from the asteroid light curves applying periodogram-type

tools. Lambda (*λ*) and Beta (*β*) are the ecliptic coordinates towards which the spin axis of the asteroid points, being *λ* the ecliptic longitude ($0° < λ ≤ 360°$), and *β* the ecliptic latitude ($−90° ≤ β ≤ 90°$). With the pole solution (*λ*, *β*) and the asteroid's inclination (i), longitude of the ascending node (Ω) and the argument of pericentre (*ω*), the obliquity (*ε*) is then obtained. In the case of $0° ≤ ε ≤ 90°$, the asteroid will have a prograde rotation and retrograde otherwise ($90° < ε ≤ 180°$). It is possible to obtain a pole ambiguity for *λ*, that is, we could obtain two solutions with almost the same value for *β*, and a pair of values for *λ* that differ ∼180° between each other.

In this work, we used our new light curves presented in Section 2, along with available sets of archival light curves. All the archival light curves were obtained from the DAMIT and Asteroid Light curve Data Exchange Format (ALCDEF; Stephens & Warner (2018); Warner, Stephens & Harris (2011); Stephens, Warner & Harris (2010)) data bases. In Tables A1, A2, A3, and A4, we summarize the archival light curves used for each asteroid.

We applied the light curve inversion method to the set of light curves for each asteroid with two codes. The first one (No YORP code) was utilized. e.g. in Ďurech, Sidorin & Kaasalainen (2010) or Hanuš et al. (2011). It generates models with constant *P* and is publicly available at the DAMIT website. The second code used (YORP code) is a modification of the former, which allows for linear
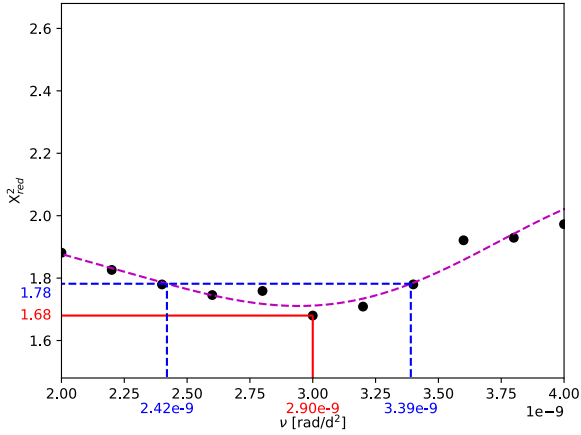
Figure 4. Variation of $\chi^2_{\rm red}$ of the fit for different models of (2100) Ra-Shalom, keeping fixed the best pole solution and varying υ from 2 to 4×10^{-9}. The lowest $\chi^2_{\rm red}$ value is at $\upsilon = 0.29 \times 10^{-8}$, with $\chi^2_{\rm red} = 1.68$ (red solid lines). The 3σ value corresponds to $\chi^2_{\rm red} = 1.78$ and is reached at $\upsilon = 0.24 \times 10^{-8}$ and 0.34×10^{-8} rad d^{-2} (blue dashed lines).
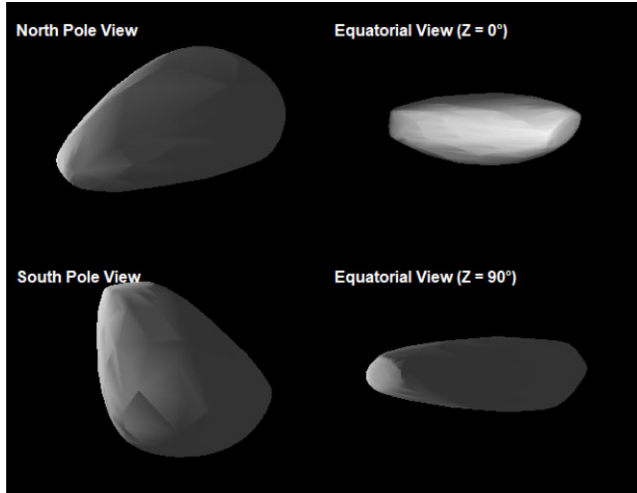
Figure 5. Linearly increasing rotation period shape model of (3103) Eger. Left top: North Pole View (Y-axis $= 0°$). Left bottom: South Pole View (Y-axis $= 180°$). Right top and bottom: Equatorial views with Z-axis rotated $0°$ and $90°$.

evolution in P over time, thus allowing to detect if the asteroid exhibits the YORP effect. It was gently provided by Josef Ďurech in personal communication; since it is not publicly available, the code was used in previous studies as Ďurech et al. (2012).

For each asteroid, we applied the following procedure independently with the No YORP and the YORP codes; First, we obtained a medium-resolution solution searching for λ and β values in all the sphere ($0° < \lambda \leq 360°$, $-90° \leq \beta \leq 90°$) with $5°$ steps and adopting as initial value for P, the previously accepted value (except for (12711) Tukmit, for which we used the P found with the period search tool implemented in the DAMIT code). Secondly, we performed a fine pole search with $2°$ steps in a $30° \times 30°$ square centred on the previous solution and starting with the P obtained in the previous search. The initial parameters for modelling were set to their default (and recommended) values; in the case of the YORP code, the YORP value was set to $\upsilon = 1 \times 10^{-8}$. Only the convexity regularization weight was modified in order to maintain the dark facet area below 1 per cent when needed. After running both codes, we reduce the

solution's χ^2 given by the code, to the number of measurements for each asteroid, obtaining a $\chi^2_{\rm red}$ value, selecting as a final solution the one with the lowest $\chi^2_{\rm red}$ value.

To obtain the uncertainties of the solution, we opted for creating 100 subsets from the main set of measurements that was used to obtain the best-fitting solution in terms of $\chi^2_{\rm red}$. To create this subsets, we removed randomly 10 or 25 per cent of the measurements from the initial set depending on its measurement number. We then recalculated the best-fitting solution for each of this new subsets, repeating the fine pole search, thus obtaining 100 solutions. With this 100 solutions, we then calculated the mean (which is almost identical to the best-fitting solution using the initial set of measurements) and standard deviation (3σ level) which are the uncertainty of the solution.

Furthermore, we applied the method proposed in Vokrouhlický et al. (2017) to alternatively obtain the uncertainty in the YORP effect at the 3σ level. For that we iterated the YORP code with all parameters, besides the YORP effect, fixed at the initial best-fitting solution values, modifying only the υ parameter and finally adopting as the final solution the one corresponding to the lowest $\chi^2_{\rm red}$ value (see Fig. 7 as an example).

4 RESULTS AND DISCUSSION

We proceed now to show the results obtained following the methods proposed in Section 3 with a discussion for each asteroid (see Table 2 for a summary of the values obtained).

4.1 (2100) Ra-Shalom

In previous studies (Kaasalainen et al. 2004; Ďurech et al. 2012, 2018), a rotation state parameters of $P = 19.8200 \pm 0.0003$ h, $\lambda = 295° \pm 15°$, and $\beta = -65° \pm 10°$ were reported as the most probable solution, and no YORP effect was detected. In these previous works, 105 light curves from Ostro et al. (1984), Harris et al. (1992), Pravec, Wolf & Šarounová (1998), Kaasalainen et al. (2004), and Ďurech et al. (2012, 2018) were used, spanning from 1978 to 2016.

We applied the inversion algorithm to 93 archival light curves and our seven new light curves acquired during 2022 (see Tables 1 and A1). First of all we ran the No YORP code since no linear evolution of P was previously reported. Fig. 1 shows the shape model obtained with this code, corresponding to a pole solution $\lambda = 278°$, $\beta = -60°$, $\epsilon \simeq 164°$, and a rotation period of $P = 19.820056$ h. The fit between the model and the data results in $\chi^2_{\rm red} = 1.66$ normalized to the 4987 data points (See Fig. B1).

Next, we performed the inversion with the YORP code, obtaining the shape model presented in Fig. 2, with the pole solution $\lambda = 283°$, $\beta = -62°$, $\epsilon \simeq 165°$, a rotation period of $P = 19.820101$ h (corresponding to 12 September 1978) and a YORP acceleration $\upsilon = 0.19 \times 10^{-8}$ rad d^{-2}. In this case, the fit between the model and the data was slightly better, resulting in $\chi^2_{\rm red} = 1.64$ normalized to the 4987 data points (See Fig. B2). In Fig. 3, we show the fits between the constant period (No YORP) and linearly increasing period (YORP) models for Ra-Shalom and the data corresponding to several seasons of observations.

The photometric data set is large ($\sim$5000 measurements), so as explained before, we estimated the mean final values of the rotation state parameters (P, λ, β) with their uncertainties repeating the modelling around the best solution with 100 subsets, removing 25 per cent of the points in each subset. For the constant period model of Ra-Shalom model, we found $P = 19.820056 \pm 0.000012$ h, $\lambda = 278° \pm 18°$, $\beta = -60° \pm 8°$, $\epsilon = 162° \pm 10°$, and for the linear
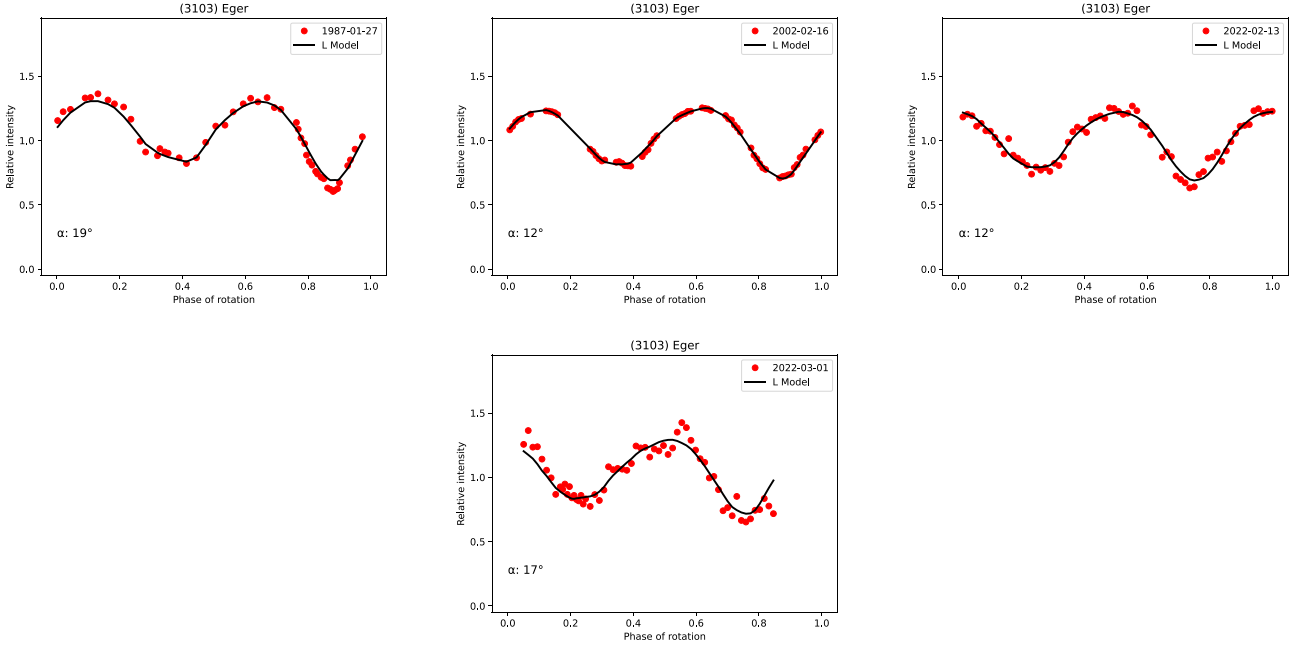
Figure 6. Four examples of the fit between dense light curves of (3103) Eger and the best-fitting linearly increasing period model (L Model). The data is plotted as red dots for each observation, meanwhile the model is plotted as a solid black line. The geometry is described by its solar phase angle α.
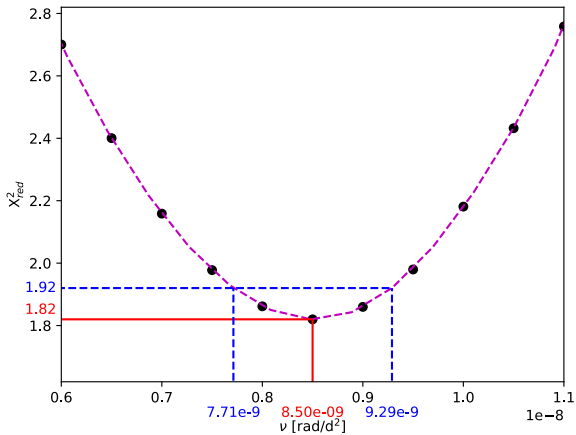

Figure 7. Variation of $\chi^2_{\rm red}$ of the fit for different models of (3103) Eger, keeping fixed the best pole solution and varying υ from 0.6 to 1.1×10^{-8}. The lowest $\chi^2_{\rm red}$ value is at $\upsilon = 0.85 \times 10^{-8}$, with $\chi^2_{\rm red} = 1.82$ (red solid lines). The 3σ value corresponds to $\chi^2_{\rm red} = 1.92$, which is reached at $\upsilon = 0.77 \times 10^{-8}$ and 0.93×10^{-8} rad d^{-2} (blue dashed lines).

increasing period model, we found $P = 19.820107 \pm 0.000040$ h, $\lambda = 278° \pm 8°$, $\beta = -60° \pm 5°$, $\epsilon = 165° \pm 5°$, and a YORP acceleration of $\upsilon = (0.22 \pm 0.16) \times 10^{-8}$ rad d^{-2}. We also estimated the uncertainty of the YORP effect in the event it is present at the 3σ level iterating the YORP code with all parameters, besides the YORP effect, fixed in the previous best solution. In this particular case, we decided to run it from 0 to 0.5×10^{-8} in 0.02×10^{-8} steps, in accordance with the low υ value derived from the computed model. With this method, we obtain $\upsilon = (0.29 \pm 0.05) \times 10^{-8}$ rad d^{-2} (see Fig. 4).

Following Rozitis & Green (2013), it is possible to estimate the expected YORP acceleration acting on a NEA from a statistical approach knowing its diameter (in km), semimajor axis (in au), and ec-

centricity computing $|d\omega/dt| = 1.20^{+1.66}_{-0.86} \times 10^{-2} (a^2\sqrt{1-e^2}D^2)^{-1}$. Adopting for Ra-Shalom, a mean diameter of $D = 1.76$ km from NEOWISE data (Masiero et al. 2021), a semimajor axis $a = 0.8321$ au, and eccentricity $e = 0.4365$, we obtain an estimated value for the YORP acceleration of $\upsilon = 4.7^{+6.5}_{-3.3} \times 10^{-8}$ rad d^{-2}, one-order of magnitude greater than the estimated value from the linearly increasing period code. If we use the diameter estimated from radar physical models (Shepard et al. 2008a) of $D = 2.9$ km, we obtain an estimate of $\upsilon = 1.7^{+2.4}_{-1.2} \times 10^{-8}$ rad d^{-2}, which is again one-order of magnitude greater than our obtained value. Obviously, more observations are necessary to confirm or discard our preliminary result. Anyway, for our estimated value of υ, it is worth computing the characteristic time-scale $T_{\rm yorp} = \omega/\upsilon$, which is the time needed to change the rotation rate of the asteroid significantly. We find that Ra-Shalom may decrease its rotation period to one-half ($\sim$10 h) in about 400 Myr. As this rotation rate is well above the break-up limit, (2100) Ra-Shalom should not experience structural changes in the next 500 Myr due to this effect.

Both linear increasing period and constant period models are a good fit with the data, being slightly better considering an acceleration of the period. It is believed that the YORP effect is responsible for the bimodality in the rotation periods observed in small asteroids, showing greater populations of fast and slow rotators (Pravec & Harris 2000). Interestingly, all asteroids with reported YORP effect to date show acceleration, which could be a bias since they all have fast rotation periods and are therefore easier to study. However, Ra-Shalom is a case of interest because it has a considerably slower rotation period ($\sim$19 h). Yet, the data suggests an acceleration instead of deceleration, being decelerated is a result that would not be unusual given its slow rotation rate. This could also suggest that the YORP effect is more efficient at accelerating than decelerating (Statler et al. 2013). Another hint of the presence of this effect on Ra-Shalom is the value of the ecliptic latitude for its spin pole; we know that another consequence of this effect is to bring the rotation axis to
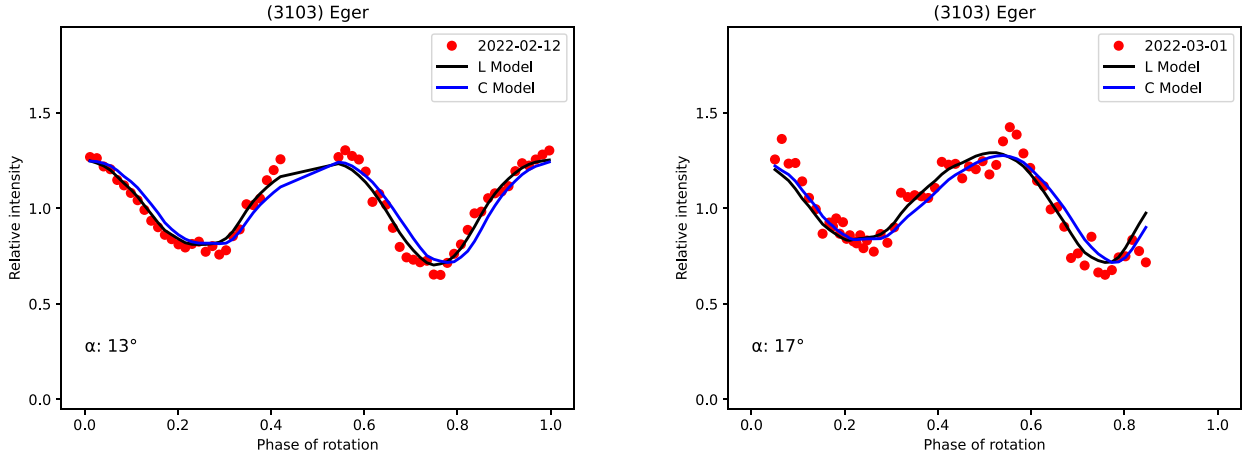
Figure 8. Example of light curves showing the offset of the fit of constant period model (C Model) to both the linearly increasing period model (L model) and the data for (3103) Eger. The data is plotted as red dots for each observation, meanwhile the C Model is plotted as a solid black line and the L Model as a solid blue line. The geometry is described by its solar phase angle α.
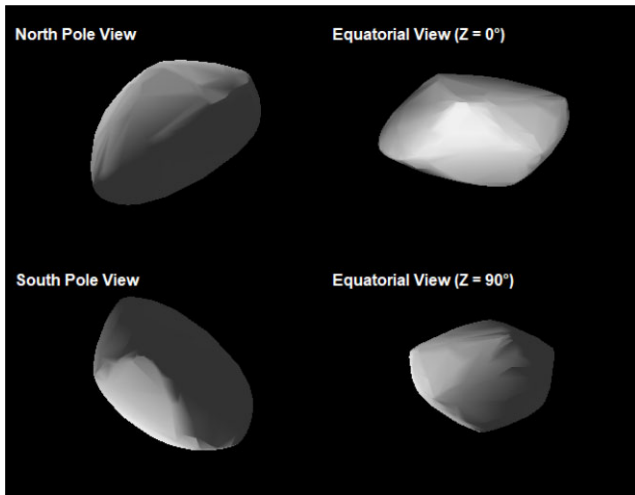
Figure 9. Constant rotation period shape model of (12711) Tukmit. Left top: North Pole View (Y-axis = 0°). Left bottom: South Pole View (Y-axis = 180°). Right top and bottom: Equatorial views with Z-axis rotated 0° and 90°.

extreme obliquity values (Hanuš et al. 2013a), so a value of $\epsilon = 165°$ suggests that this effect could be taking place.

4.2 (3103) Eger

Previous studies have focused on (3103) Eger (Ďurech et al. 2009a, 2012, 2018), detecting the presence of the YORP effect. The most recent study (Ďurech et al. 2018) reports the following rotation state parameters: $P = 5.710156 \pm 0.000007$ h, $\lambda = 226° \pm 15°$, $\beta = -70° \pm 4°$, and $\upsilon = (1.4 \pm 0.6) \times 10^{-8}$ rad d^{-2}, from a total of 72 dense light curves. In this work, we used our ten new light curves (see Table 1) along with 80 archival light curves published by Wisniewski (1987, 1991), Velichko, Kruglyj & Chernyj (1992), Pravec, Wolf & Šarounová (1998), Ďurech et al. (2012, 2018), and Warner (2017) (see Table A2 for a summary of the archival light curves).

We computed a model with the YORP code since the effect was already reported. For that, we used 90 light curves with a temporal span of 36 years (1986–2022), finding as best solution: $\lambda = 214°$,

$\beta = -71°$, $\epsilon \simeq 177°$, rotation period corresponding to 1986 July 6 (date of the very first observation in the data set) $P = 5.710148$ h, and a YORP acceleration $\upsilon = 0.847 \times 10^{-8}$ rad d^{-2}. The fit between model and data corresponds to a value of $\chi^2_{red} = 1.74$ normalized to the 6034 data points (see Figs 6 and B3). In Fig. 5, we show the shape model of (3103) Eger.

We recomputed the model around the best solution with 100 subsets, each removing 25 per cent of the points ($\sim$6000 measurements). We obtained the following final values: $P = 5.710148 \pm 0.000006$ h, $\lambda = 214° \pm 3°$, $\beta = -71° \pm 1°$, $\epsilon = 177° \pm 1°$, and YORP acceleration $\upsilon = (0.85 \pm 0.05) \times 10^{-8}$ rad d^{-2}.

We employed also the 3σ method to obtain a second estimation of the uncertainty of υ, iterating the υ value from 0 to 3×10^{-8} in 0.05×10^{-8} steps, and maintaining the rest of the values fixed at the best solution values (see Fig. 7). In this way, we obtained $\upsilon = (0.85 \pm 0.08) \times 10^{-8}$ rad d^{-2}, which is in agreement with the previous computed value.

We also computed a shape model with constant period obtaining the following values: $\lambda = 218°$, $\beta = -71°$, $\epsilon \simeq 178°$, rotation period $P = 5.710136$ h with $\chi^2_{red} = 2.95$ (Fig. 8 shows the fit of both models to some example light curves). The χ^2_{red} value is higher than the linearly increasing period shape model solution ($\chi^2_{red} = 1.74$) previously obtained, thus we conclude that our linearly increasing period model for (3103) Eger confirms and refines the previous values for its spin parameters and their uncertainties.

For (3103) Eger, we estimated a value $T_{yorp} = \omega/\upsilon$ of $\sim$8 Myr, time it would take the asteroid to decrease its rotation period to $\sim$2.8 h, close to the critical rotation period of $\sim$2 h, meaning that significant structural changes could take place within this typical time-scale.

4.3 (12711) Tukmit

Previous studies of this NEA only measured its rotation period, obtaining $P = 3.4848 \pm 0.0001$ h in Warner & Stephens (2022) and Pravec (2000web).[9] With our three new dense light curves (see Table 1) and two archival light curves from ALCDEF (see Table A3), we derived the first spin and shape model for (12711) Tukmit.

Due to the short temporal window of the observations (less than one year), we computed a constant period model, obtaining a period

---

[9] https://www.asu.cas.cz/ppravec/newres.txt
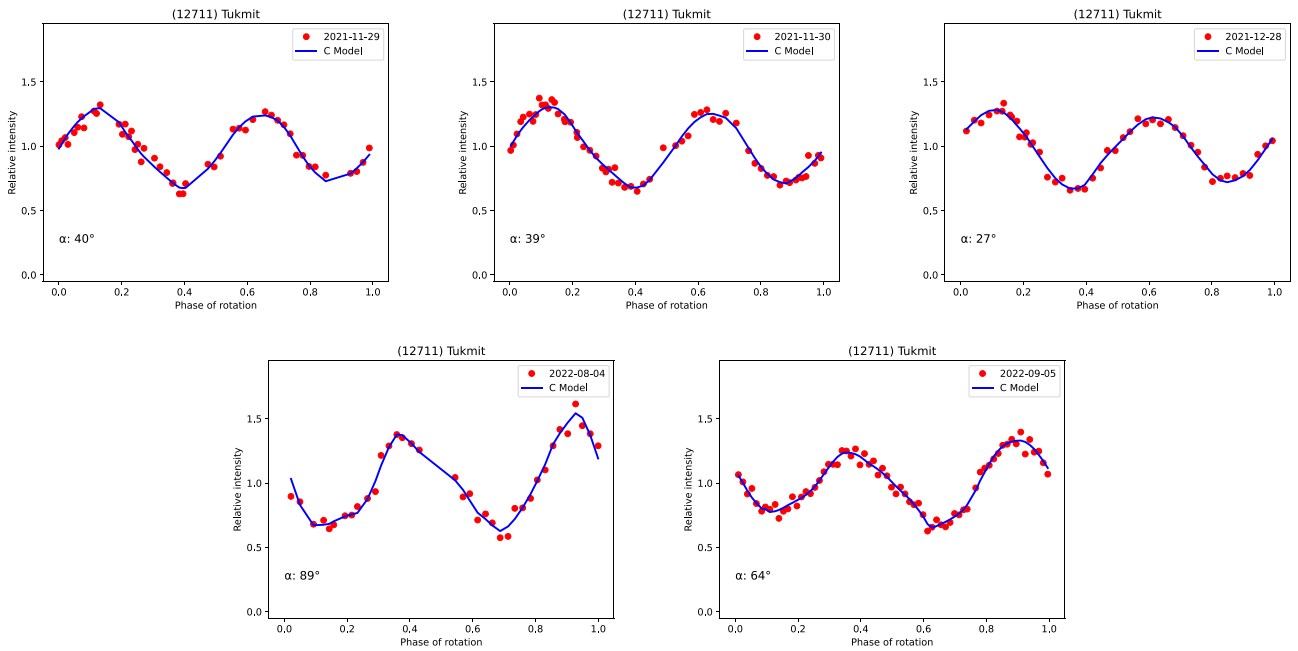
Figure 10. Fits between all the light curves of (12711) Tukmit with the best-fitting constant period model (C Model). The data is plotted as red dots for each observation, meanwhile the model is plotted as a solid blue line. The geometry is described by its solar phase angle α.
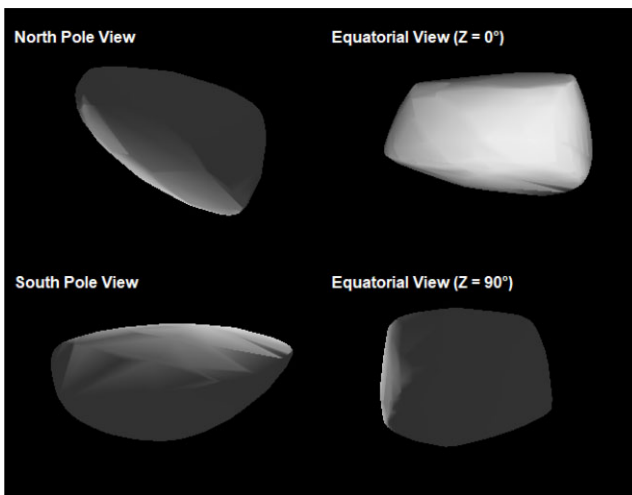
Figure 11. Linearly increasing rotation period shape model of (161989) Cacus. Left top: North Pole View (Y-axis $= 0°$). Left bottom: South Pole View (Y-axis $= 180°$). Right top and bottom: Equatorial Views with Z-axis rotated $0°$ and $90°$.

of $P = 3.484895$ h with a pole orientation $\lambda = 27°$, $\beta = 11°$, and $\epsilon \simeq 118°$. In Fig. 9, we show the shape model for this solution. The fit between model and data has in this case $\chi^2_{\text{red}} = 1.06$ (see Figs 10 and B4).

To estimate the mean values and their uncertainties, since the main data set for Tukmit is smaller compared to the others (~ 150 measurements), we decided to remove 10 per cent of the main data to obtain each subset instead of 25 per cent. We obtained $P = 3.484900 \pm 0.000031$ h, $\lambda = 27° \pm 8°$, $\beta = 9° \pm 15°$, and $\epsilon = 119° \pm 15°$.

Since the time span of the observations is so small (~ 1 yr), it is extremely unlikely that we would detect the YORP effect, if it

were present, unless being extremely strong. Anyway, we computed a linear increasing period model, but as expected, the obtained best-fitting model was unsuccessful to improve the constant P model. We note that the aforementioned obliquity expected in a YORP affected asteroid is not present in the best-fitting model obtained ($\epsilon \simeq 118°$). Anyway, according to Rozitis & Green (2013), we could expect a YORP acceleration of $\nu = 1.8^{+2.5}_{-1.3} \times 10^{-8}$ rad d^{-2}, assuming $D = 1.94$ km (Trilling et al. 2010), $a = 1.1863$ au, and e $= 0.2721$. If so, the value $T_{\text{yorp}} = \omega/\nu$ would be ~ 8 Myr, time at which the asteroid would reach a rotation period of ~ 1.7 h, well beyond the critical rotation limit. More observations are needed to confirm and refine our results for (12711) Tukmit.

4.4 (161989) Cacus

This asteroid has been already studied in Ďurech et al. (2018), being reported to be affected by YORP. The published parameters are $P = 3.755067 \pm 0.000002$ h (for the first observation of February 28 1978), $\lambda = 254° \pm 5°$, $\beta = -62° \pm 2°$, and $\nu = (1.9 \pm 0.3) \times 10^{-8}$ rad d^{-2}. To compute that model, a set of 22 light curves was used (see Table A4), spanning from 1978 to 2016.

We added to those previous observations, our three new light curves acquired during 2022 (see Table 1), increasing to 44 years the temporal window of the observations. We computed a linearly increasing period model since the YORP effect has been previously reported for (161989) Cacus. The best-fitting solution corresponds to a pole orientation of $\lambda = 251°$, $\beta = -61°$, $\epsilon \simeq 178°$, $P = 3.755067$ h (corresponding to February 28, 1978) and a YORP acceleration $\nu = 1.91 \times 10^{-8}$ rad d^{-2}. The fit between the model and data corresponds to a value of $\chi^2_{\text{red}} = 1.31$ normalized to the 1534 data points. In Fig. 11, we show the associated shape model (see Fig. 12 for a graphical representation of the fit).

To obtain the final mean values and their uncertainties for each parameter of the model, we recomputed the model for 100 subsets obtained removing randomly 25 per cent of the data from the main
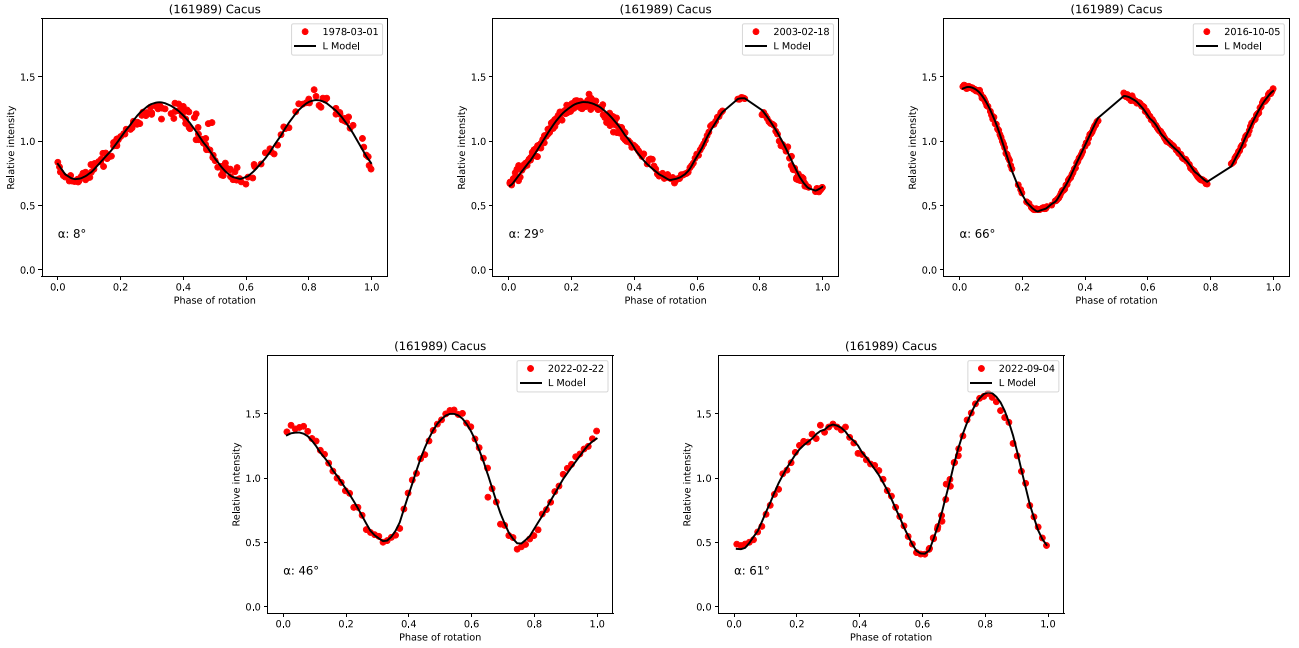
Figure 12. Fits between five light curves of (161989) Cacus and the best-fitting linearly increasing period model (L Model). The data is plotted as red dots for each observation, meanwhile the model is plotted as a solid black line. The geometry is described by its solar phase angle α.
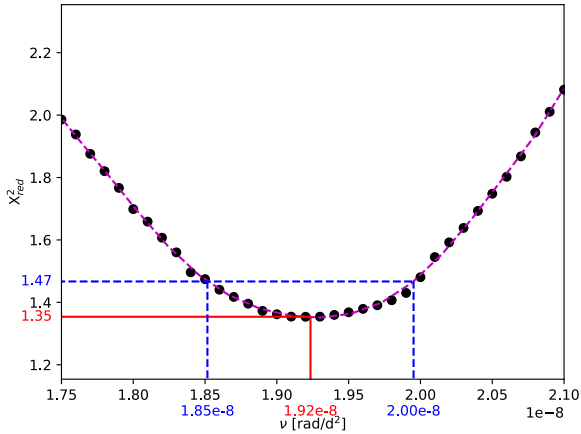
Figure 13. Variation of $\chi^2_{\rm red}$ of the fit for different models of (161989) Cacus, keeping fixed the best pole solution and varying υ from 1.75 to 2.1×10^{-8}. The lowest $\chi^2_{\rm red}$ value is at $\upsilon = 1.92 \times 10^{-8}$, with $\chi^2_{\rm red} = 1.35$ (red solid lines). The 3σ value corresponds to $\chi^2_{\rm red} = 1.47$, which is reached at $\upsilon = 1.85 \times 10^{-8}$ and 2.00×10^{-8} rad d^{-2} (blue dashed lines).

set (in this case the number of measurements is large enough $\sim$1500 measurements). We obtained $P = 3.755067 \pm 0.000001$ h, $\lambda = 251°$ $\pm 6°$, $\beta = -62° \pm 2°$, $\epsilon = 177° \pm 2°$, and $\upsilon = (1.91 \pm 0.05) \times 10^{-8}$ rad d^{-2}.

We also used the 3σ method to estimate the uncertainty of the YORP effect, iterating in this case, the υ value between 0 and 3×10^{-8} with 0.01×10^{-8} steps. In this way, we find $\upsilon = (1.92 \pm 0.08) \times 10^{-8}$ rad d^{-2} (see Figs 13 and B5), in good agreement with the best-fitting model.

As for (3103) Eger, we also computed a shape model with constant period, obtaining the following values: $\lambda = 245°$, $\beta = -61°$, $\epsilon \simeq 176°$ rotation period $P = 3.755052$ h and $\chi^2_{\rm red} = 13.65$ (Fig. 14 shows the fit of both models to some example light curves). The $\chi^2_{\rm red}$ value is much higher than the linearly increasing period shape

model ($\chi^2_{\rm red} = 1.31$) previously obtained, thus, we conclude that our results for (161989) Cacus confirm previous works and significantly decrease the uncertainty of the υ value.

We also estimate $T_{\rm yorp} = \omega/\upsilon \sim 8.2$ Myr, time-scale at which the asteroid would reach a rotation period of $\sim$1.9 h, which is beyond the critical rotation period.

5 CONCLUSIONS

In this work, we computed models, spin state and shape, including period changes due to YORP for asteroids (2100) Ra-Shalom, (3103) Eger, (12711) Tukmit, and (161989) Cacus. For asteroids (3103) Eger and (161989) Cacus, our results agree with those published by Ďurech et al. (2012, 2018), obtaining smaller uncertainties. For (3103) Eger, we found $P = 5.710148 \pm 0.000006$ h, $\lambda = 214° \pm 3°$, $\beta = -71° \pm 1°$, $\epsilon = 177° \pm 1°$, and YORP acceleration $\upsilon = (0.85 \pm 0.05) \times 10^{-8}$ rad d^{-2}. For (161989) Cacus, our best-fitting rotation state parameters are: $P = 3.755067$ h, $\lambda = 251°$ $\pm 6°$, $\beta = -62° \pm 2°$, $\epsilon = 177° \pm 2°$, and a YORP acceleration $\upsilon = (1.91 \pm 0.05) \times 10^{-8}$ rad d^{-2}.

For (2100) Ra-Shalom, while the rotation state parameters (P, λ, β) agree with the results proposed in Ďurech et al. (2018), we can not discard a hint of YORP acceleration taking place, since the best-fitting model with linearly increasing rotation period has a slightly lower $\chi^2_{\rm red}$ value and uncertainties than the constant period model. We obtained using a constant period model: $P = 19.820056 \pm 0.000012$ h, $\lambda = 278° \pm 18°$, $\beta = -60° \pm 8°$, and $\epsilon = 162° \pm 10°$, meanwhile the values obtained for this asteroid with a linear increasing period are: $\lambda = 278° \pm 8°$, $\beta = -60° \pm 5°$, $\epsilon = 165° \pm 5°$ with a rotation period of $P = 19.820107 \pm 0.000040$ h and YORP acceleration $\upsilon = (0.22 \pm 0.16) \times 10^{-8}$ rad d^{-2}. It is also worth mentioning that to compute the uncertainties a 100 models were created in a $30° \times 30°$ square centred around the best-fitting solution, obtaining values near the solution and always positive. If so, (161989) Ra-Shalom would be the slowest rotator of the known
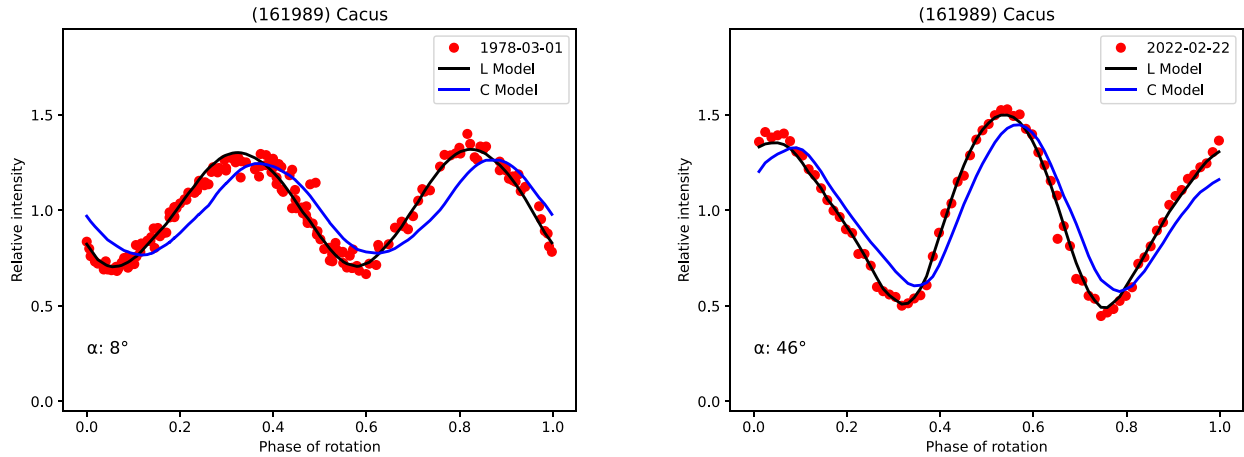
Figure 14. Example of light curves showing the offset of the fit of constant period model (C Model) to both the linearly increasing period model (L model) and the data for (161989) Cacus. The data is plotted as red dots for each observation, meanwhile the C Model is plotted as a solid black line and the L Model as a solid blue line. The geometry is described by its solar phase angle α.

asteroids with YORP detection. Furthermore, this could also be a hint that this effect is more effective accelerating than decelerating.

Finally, for asteroid (12711) Tukmit, we present the first shape model and rotation state parameters (P, λ, β) from a limited set of light curves, confirming and refining the period published by Warner & Stephens (2022), and finding $P = 3.484900 \pm 0.000031$ h, $\lambda = 27° \pm 8°$, $\beta = 9° \pm 15°$, and $\epsilon = 119° \pm 15°$.

DATA AVAILABILITY

The data underlying this article will be shared on reasonable request to the corresponding author.

REFERENCES

Alarcon M. R., Licandro J., Serra-Ricart M., Joven E., Gaitan V., de Sousa R., 2023, Publ. Astron. Soc. Pac., 135, 055001
Benner L. A. M. et al., 1997, Icarus, 130, 296
Benner L. A. M. et al., 2008, Icarus, 198, 294
Bottke William F. J., Vokrouhlický D., Rubincam D. P., Nesvorný D., 2006, Annu. Rev. Earth Planet., 34, 157
Chesley S. R. et al., 2003, Science, 302, 1739
Degewij J., Lebofsky L., Lebofsky M., 1978, IAU Circ., 3193, 1
Ďurech J. et al., 2007, A&A, 465, 331
Ďurech J. et al., 2008, A&A, 489, L25
Ďurech J. et al., 2009a, American Astronomical Society, DPS meeting #41, 56.04
Ďurech J. et al., 2009b, A&A, 493, 291
Ďurech J. et al., 2012, A&A, 547, A10
Ďurech J. et al., 2018, A&A, 609, A86
Ďurech J., Hanuš J., Oszkiewicz D., Vančo R., 2016, A&A, 587, A48
Ďurech J., Hanuš J., Vančo R., 2019, A&A, 631, A2
Ďurech J., Sidorin V., Kaasalainen M., 2010, A&A, 513, A46
Hanuš J. et al., 2011, A&A, 530, A134
Hanuš J. et al., 2013a, A&A, 551, A67
Hanuš J. et al., 2013b, A&A, 559, A134
Harris A. W., Young J. W., Dockweiler T., Gibson J., Poutanen M., Bowell E., 1992, Icarus, 95, 115
Heinze A. N. et al., 2018, AJ, 156, 241
Kaasalainen M. et al., 2004, Icarus, 167, 178
Kaasalainen M., Ďurech J., Warner B. D., Krugly Y. N., Gaftonyuk N. M., 2007, Nature, 446, 420
Kaasalainen M., Torppa J., 2001, Icarus, 153, 24
Kaasalainen M., Torppa J., Muinonen K., 2001, Icarus, 153, 37
Kochanek C. S. et al., 2017, PASP, 129, 104502
Koehn B. W., Bowell E. G., Skiff B. A., Sanborn J. J., McLelland K. P., Pravec P., Warner B. D., 2014, Minor Planet Bulletin, 41, 286
Licandro J. et al., 2023, MNRAS, 521, 3784
Lowry S. C. et al., 2007, Science, 316, 272
Lowry S. C. et al., 2014, A&A, 562, A48
Masiero J. R., Mainzer A. K., Bauer J. M., Cutri R. M., Grav T., Kramer E., Pittichová J., Wright E. L., 2021, psj, 2, 162
Mommert M., 2017, Astron. Comput., 18, 47

Morbidelli A., Vokrouhlický D., 2003, Icarus, 163, 120
O'Keefe J., 1976, Exp. Neurol., 51, 78
Ostro S. J., Harris A. W., Campbell D. B., Shapiro I. I., Young J. W., 1984, Icarus, 60, 391
Paddack S. J., 1969, J. Geophys. Res., 74, 4379
Parley N. R. et al., 2005, Earth Moon Planets, 97, 261
Pravec P. et al., 2008, Icarus, 197, 497
Pravec P., Harris A. W., 2000, Icarus, 148, 12
Pravec P., Wolf M., Šarounová L., 1998, Icarus, 136, 124
Radzievskii V. V., 1952, Astron. Zh., 29, 162
Rozitis B., Green S. F., 2013, MNRAS, 430, 1376
Schuster H. E., Surdej A., Surdej J., 1979, A&AS, 37, 483
Shepard M. K. et al., 2008a, Icarus, 193, 20
Shepard M. K. et al., 2008b, Icarus, 195, 184
Shepard M. K., Benner L. A. M., Ostro S. J., Harris A. W., Rosema K. D., Shapiro I. I., Chandler J. F., Campbell D. B., 2000, Icarus, 147, 520
Slivan S. M., 2002, Nature, 419, 49
Statler T. S., Cotto-Figueroa D., Riethmiller D. A., Sweeney K. M., 2013, Icarus, 225, 141
Stephens R. D., Warner B. D., Harris A. W., 2010, American Astronomical Society, DPS meetings #42, 39.14
Stephens R., Warner B. D., 2018, American Astronomical Society, DPS meeting #50, 417.03
Taylor P. A. et al., 2007, Science, 316, 274
Tonry J. L. et al., 2018, PASP, 130, 064505
Torppa J., Kaasalainen M., Michałowski T., Kwiatkowski T., Kryszczyńska A., Denchev P., Kowalski R., 2003, Icarus, 164, 346
Trilling D. E. et al., 2010, AJ, 140, 770
Velichko F. P., Kruglyj Y. N., Chernyj V. G., 1992, Astronomicheskij Tsirkulyar, 1553, 37
Vokrouhlický D. et al., 2017, AJ, 153, 270
Vokrouhlický D., Bottke W. F., Chesley S. R., Scheeres D. J., Statler T. S., 2015, in MichelP., DeMeoF. E., BottkeW. F., eds, Asteroids IV. University of Arizona Press, Tucson, p. 509
Walsh K. J., Richardson D. C., Michel P., 2008, Nature, 454, 188
Warner B. D., 2017, Minor Planet Bull., 44, 223
Warner B. D., Stephens R. D., 2022, Minor Planet Bulletin, 49, 83
Warner B. D., Stephens R. D., Harris A. W., 2011, Minor Planet Bulletin, 38, 172
Wisniewski W. Z., 1987, Icarus, 70, 566
Wisniewski W. Z., 1991, Icarus, 90, 117
Yarkovsky I., 1901, The Density of Luminiferous Ether and the Resistance it Offers to Motion. Bryansk, Russia

APPENDIX A: SUMMARY OF ARCHIVAL LIGHT CURVES USED IN THIS WORK

Table A1. Archival observations for (2100) Ra-Shalom. The information includes the date, the starting and end time (UT) of the observations, the phase angle (α), the heliocentric (r) and geocentric (Δ) distances, phase angle bisector longitude (PABLon) and latitude (PABLat) of the asteroid at the time of observation. **References:** HAR92: Harris et al. (1992); OST84: Ostro et al. (1984); PRA98: Pravec, Wolf & Šarounová (1998); KAA04: Kaasalainen et al. (2004); DUR12: Ďurech et al. (2012); DUR18: Ďurech et al. (2018).

Date	UT (start)	UT (end)	$\alpha[°]$	r [au]	Δ [au]	PABLon [°]	PABLat [°]	Reference
1978-Sep-12	05:35:59.971	0:12:00.000	3.06	1.1945	0.1884	348.549	1.9168	HAR92
1981-Aug-25	05:42:09.504	1:36:28.224	30.63	1.1624	0.1811	331.617	20.5476	OST84
1981-Aug-28	08:43:20.352	0:58:24.672	28.07	1.1696	0.1851	329.838	18.231	OST84
1981-Sep-02	03:47:02.688	8:58:09.408	27.63	1.1789	0.1965	327.606	14.644	OST84
1997-Aug-30	21:34:59.002	3:02:03.638	41.27	1.1952	0.2677	8.1616	2.7398	PRA98
1997-Sep-01	21:58:07.190	2:55:50.995	39.06	1.1949	0.256	8.1911	1.8904	PRA98
1997-Sep-02	21:35:20.602	3:09:22.550	37.93	1.1945	0.2504	8.1712	1.4562	PRA98
1997-Sep-03	23:02:59.251	3:14:06.979	36.65	1.1941	0.2445	8.1231	0.9737	PRA98
1997-Sep-06	00:28:43.853	3:22:17.126	34.02	1.193	0.2333	7.9446	− 0.0099	PRA98
1997-Sep-11	21:23:44.304	3:35:41.165	25.57	1.1876	0.2051	6.7514	− 3.1789	PRA98
2000-Aug-23	19:55:14.246	3:23:03.754	34.82	1.1791	0.2137	351.287	13.6909	KAA04
2000-Aug-24	00:26:36.672	5:56:32.986	34.49	1.1794	0.213	351.217	13.6175	KAA04
2000-Aug-24	22:46:46.301	4:26:49.142	32.81	1.1809	0.21	350.867	13.233	KAA04
2000-Aug-25	20:57:49.795	2:45:19.325	31.1	1.1824	0.2072	350.494	12.8392	KAA04
2000-Aug-26	19:35:11.818	2:52:43.939	29.32	1.1838	0.2045	350.088	12.4257	KAA04
2000-Aug-27	04:34:47.280	5:53:59.280	28.6	1.1843	0.2035	349.913	12.2629	KAA04
2003-Aug-06	19:17:10.003	0:46:24.499	63.99	1.0826	0.1881	333.888	37.2542	DUR12
2003-Aug-24	00:03:29.952	0:22:04.166	37.87	1.1474	0.1802	323.434	24.2987	DUR12
2003-Aug-24	21:57:08.179	1:25:21.101	37.15	1.15	0.182	323.002	23.4851	DUR12
2003-Aug-25	21:39:35.136	0:50:24.778	36.51	1.1528	0.1842	322.561	22.6059	DUR12
2003-Aug-27	17:52:42.902	0:16:37.229	35.69	1.1578	0.189	321.831	20.9753	DUR12
2003-Aug-29	17:46:55.661	0:51:28.800	35.32	1.1628	0.1952	321.173	19.2443	DUR12
2003-Aug-30	18:03:19.930	0:04:23.952	35.32	1.1653	0.1988	320.894	18.3859	DUR12
2003-Aug-31	23:51:33.264	0:18:39.312	35.49	1.1681	0.2034	320.593	17.3552	DUR12
2003-Sep-02	21:41:22.272	0:08:19.997	36	1.1722	0.2113	320.245	15.8157	DUR12
2003-Sep-05	21:15:57.312	3:08:13.747	37.31	1.1779	0.225	319.928	13.5496	DUR12
2003-Sep-06	22:08:17.952	3:12:01.930	37.87	1.1797	0.2302	319.878	12.8038	DUR12
2003-Sep-14	20:06:33.955	1:01:11.885	42.75	1.1901	0.2747	320.347	7.7938	DUR12
2003-Sep-15	18:26:53.088	0:25:59.837	43.33	1.191	0.2804	320.485	7.2794	DUR12
2003-Sep-16	18:21:37.210	0:01:37.517	43.94	1.1918	0.2866	320.647	6.7446	DUR12
2003-Sep-17	18:51:25.085	9:50:50.726	44.56	1.1925	0.293	320.829	6.2131	DUR12
2009-Aug-13	17:37:01.315	9:54:49.277	84.86	0.9792	0.3617	262.483	30.6297	DUR12
2009-Aug-14	17:35:55.046	9:44:51.130	83.83	0.9855	0.3625	263.831	30.0153	DUR12
2009-Aug-16	17:28:54.538	9:32:55.306	81.8	0.9979	0.3651	266.449	28.7684	DUR12
2009-Aug-17	17:15:11.491	9:57:09.245	80.81	1.0039	0.3668	267.712	28.1429	DUR12
2009-Aug-23	18:38:14.957	0:30:10.656	75.21	1.0385	0.3831	274.927	24.3233	DUR12
2009-Sep-19	16:30:22.723	9:14:26.275	60.83	1.1501	0.5405	298.924	10.782	DUR12
2009-Sep-20	16:28:47.510	9:08:04.474	60.55	1.1529	0.548	299.644	10.4035	DUR12
2009-Sep-21	16:31:15.341	8:58:07.018	60.28	1.1556	0.5555	300.358	10.0314	DUR12
2013-Sep-07	00:01:06.096	3:14:18.038	59.18	1.1529	0.4025	33.4915	− 8.2415	DUR18
2013-Sep-08	00:00:07.603	3:08:08.419	59.33	1.1501	0.3952	34.1256	− 8.7121	DUR18
2013-Sep-10	00:17:10.061	1:09:01.411	59.68	1.1441	0.3806	35.4226	− 9.7022	DUR18
2013-Sep-27	01:35:02.314	3:40:39.158	66.78	1.0783	0.2738	47.9848	− 21.1684	DUR18
2013-Sep-28	01:58:03.677	3:54:32.746	67.55	1.0735	0.2689	48.8524	− 22.0693	DUR18
2016-Aug-10	08:30:02.966	1:13:57.619	57.23	1.1907	0.4862	10.1379	5.1135	DUR18
2016-Aug-11	08:26:16.512	1:41:30.538	56.98	1.1916	0.4794	10.5629	4.8588	DUR18
2016-Aug-12	08:20:44.822	1:52:10.762	56.73	1.1923	0.4725	10.9843	4.6001	DUR18
2016-Aug-13	08:25:49.987	1:29:16.483	56.46	1.193	0.4655	11.4055	4.3347	DUR18
2016-Aug-14	08:21:19.814	1:49:09.667	56.2	1.1936	0.4585	11.8208	4.0662	DUR18
2016-Aug-15	08:14:47.299	1:59:42.634	55.93	1.1941	0.4515	12.2322	3.7929	DUR18
2016-Aug-16	08:46:39.418	2:03:16.646	55.64	1.1945	0.4443	12.6509	3.5067	DUR18
2016-Aug-19	09:16:34.205	0:51:48.701	54.76	1.1952	0.4228	13.8668	2.6249	DUR18
2016-Aug-20	09:13:49.786	1:36:21.053	54.45	1.1952	0.4157	14.2611	2.3207	DUR18
2016-Aug-25	23:03:40.896	2:59:53.693	52.6	1.1938	0.3757	16.3893	0.4809	DUR18
2016-Aug-27	22:55:21.763	3:00:50.112	51.86	1.1926	0.3614	17.1111	− 0.2421	DUR18
2016-Aug-29	23:49:11.741	2:51:28.771	51.06	1.191	0.3467	17.8244	− 1.0227	DUR18
2016-Aug-30	23:03:34.589	2:52:12.922	50.67	1.1901	0.3398	18.1539	− 1.4102	DUR18
2016-Sep-02	22:46:43.018	2:32:33.734	49.38	1.1868	0.3187	19.1281	− 2.6793	DUR18
2016-Sep-10	00:18:12.010	2:31:41.635	45.98	1.1758	0.2702	21.1091	− 6.2176	DUR18
2016-Sep-11	16:42:55.958	8:57:38.678	45.1	1.1726	0.2592	21.4923	− 7.1972	DUR18
2016-Sep-16	16:17:18.730	9:00:05.818	42.56	1.1613	0.2282	22.3748	− 10.4834	DUR18

Table A1 – *continued*

Date	UT (start)	UT (end)	$\alpha[°]$	r [au]	Δ [au]	PABLon [°]	PABLat [°]	Reference
2016-Sep-19	17:58:12.518	8:50:24.691	41.18	1.1532	0.2106	22.6733	− 12.8409	DUR18
2016-Sep-22	16:36:35.539	8:30:08.957	40.21	1.1447	0.1953	22.7238	− 15.3684	DUR18
2016-Sep-23	16:56:25.526	7:53:51.936	40	1.1415	0.1903	22.6801	− 16.3031	DUR18
2016-Sep-25	17:03:34.502	8:49:42.701	39.86	1.135	0.1813	22.4863	− 18.2482	DUR18
2016-Sep-26	16:43:28.963	8:51:45.216	39.95	1.1317	0.1772	22.334	− 19.2504	DUR18
2016-Sep-27	16:26:26.419	8:41:40.934	40.15	1.1283	0.1733	22.1416	− 20.2838	DUR18
2016-Oct-08	00:16:45.869	1:06:03.341	50.96	1.087	0.1503	17.4875	− 32.0972	DUR18
2016-Oct-08	07:16:18.595	8:21:30.787	51.46	1.0857	0.1502	17.2791	− 32.4224	DUR18
2016-Oct-08	08:17:40.099	9:17:18.787	51.53	1.0855	0.1502	17.2502	− 32.4695	DUR18
2016-Oct-09	01:33:02.650	2:31:11.482	52.86	1.0822	0.1499	16.7576	− 33.2909	DUR18
2016-Oct-09	08:30:40.378	9:16:35.674	53.38	1.0809	0.1499	16.5441	− 33.6065	DUR18
2016-Oct-10	01:12:32.314	2:05:34.426	54.71	1.0777	0.1499	16.0483	− 34.3862	DUR18
2016-Oct-10	02:51:36.634	3:45:13.306	54.84	1.0773	0.1499	15.9941	− 34.4603	DUR18
2016-Oct-10	04:30:26.266	5:09:16.474	54.97	1.077	0.15	15.9406	− 34.5333	DUR18
2016-Oct-10	05:04:28.762	5:35:28.954	55.02	1.0769	0.15	15.9225	− 34.5583	DUR18
2016-Oct-10	07:30:08.986	8:03:12.730	55.2	1.0764	0.15	15.8469	− 34.665	DUR18
2016-Oct-10	08:32:19.738	9:13:05.722	55.28	1.0762	0.15	15.8157	− 34.7106	DUR18
2016-Oct-13	10:17:33.418	2:27:43.891	61.44	1.0613	0.1522	13.4717	− 37.9095	DUR18
2016-Oct-13	12:23:07.411	4:23:05.654	61.62	1.0609	0.1524	13.409	− 37.9954	DUR18
2016-Oct-13	14:16:11.626	6:10:06.730	61.78	1.0605	0.1524	13.3526	− 38.0742	DUR18
2016-Oct-14	11:56:14.582	4:06:16.502	63.64	1.0559	0.1537	12.6441	− 38.9464	DUR18
2016-Oct-14	14:01:40.627	6:20:16.541	63.82	1.0554	0.1538	12.5818	− 39.0305	DUR18
2016-Oct-14	16:21:25.661	8:28:47.741	64.02	1.0549	0.1539	12.5107	− 39.1256	DUR18
2016-Oct-15	09:10:18.365	1:14:43.930	65.46	1.0513	0.155	11.9518	− 39.775	DUR18
2016-Oct-15	11:10:07.709	3:16:44.515	65.63	1.0509	0.1552	11.8922	− 39.8503	DUR18
2016-Oct-15	13:36:17.914	5:04:30.950	65.84	1.0504	0.1554	11.8204	− 39.9442	DUR18
2016-Oct-17	09:29:16.512	1:49:29.798	69.57	1.0407	0.1589	10.4243	− 41.553	DUR18
2016-Oct-17	11:39:08.237	2:38:03.034	69.75	1.0402	0.1591	10.363	− 41.6289	DUR18
2016-Oct-17	15:00:45.446	7:55:32.506	70.03	1.0394	0.1595	10.2679	− 41.7501	DUR18
2016-Oct-25	13:51:48.874	7:50:22.243	84.98	0.9934	0.1826	5.3987	− 47.5766	DUR18
2016-Oct-26	13:37:33.859	5:35:19.565	86.67	0.9872	0.1861	4.9692	− 48.2212	DUR18
2016-Oct-26	15:33:04.262	7:39:46.771	86.81	0.9867	0.1864	4.9396	− 48.2762	DUR18

Table A2. Archival observations for (3103) Eger. The information includes the date, the starting and end time (UT) of the observations, the phase angle (α), the heliocentric (r) and geocentric (Δ) distances, phase angle bisector longitude (PABLon) and latitude (PABLat) of the asteroid at the time of observation. **References:** WIS87: Wisniewski (1987); VEL92: Velichko, Kruglyj & Chernyj (1992); PRA98: Pravec, Wolf & Šarounová (1998); DUR12: Ďurech et al. (2012); WAR17: Warner (2017); DUR18: Ďurech et al. (2018).

Date	UT (start)	UT (end)	$\alpha[°]$	r [au]	Δ [au]	PABLon [°]	PABLat [°]	Reference
1986-Jul-06	07:47:25.958	0:18:09.706	44.24	1.2215	0.3206	316.316	14.1376	WIS87
1986-Jul-12	07:18:13.680	0:43:15.485	44.95	1.1887	0.2683	321.301	11.3073	WIS87
1986-Aug-07	09:38:39.581	2:37:16.032	71.09	1.0519	0.1454	352.978	− 22.2845	WIS87
1987-Jan-26	06:53:01.248	2:54:02.419	20.26	1.4193	0.4783	145.334	4.1932	WIS87
1987-Jan-27	06:06:02.016	1:54:01.958	19.28	1.4242	0.4792	145.279	4.5679	WIS87
1987-Feb-02	06:54:54.432	2:07:55.373	13.64	1.4545	0.4896	144.818	6.7972	WIS87
1991-Jul-07	20:22:11.222	0:52:58.109	41.98	1.2225	0.3046	314.682	14.7361	VEL92
1991-Jul-17	20:39:38.390	0:16:11.395	42.25	1.1677	0.2189	322.928	9.3619	VEL92
1996-Jul-14	21:49:35.616	1:42:18.720	40.29	1.1839	0.2343	319.231	11.525	PRA98
1996-Jul-16	21:29:00.096	1:52:43.392	40.22	1.1731	0.218	320.915	10.2489	PRA98
1996-Jul-19	20:01:42.182	1:20:49.978	40.26	1.1571	0.1949	323.577	8.0107	PRA98
1996-Jul-19	21:50:23.136	1:49:38.496	40.26	1.1567	0.1943	323.649	7.9468	PRA98
1996-Jul-21	22:21:37.152	1:33:29.952	40.48	1.1458	0.1794	325.621	6.0984	PRA98
1996-Jul-26	22:47:04.704	2:05:27.168	42.47	1.119	0.1468	331.076	0.0887	PRA98
1997-Feb-04	18:57:38.333	1:54:03.802	9.95	1.4576	0.4824	142.691	7.245	PRA98
1997-Feb-04	22:49:04.195	3:26:27.427	9.86	1.4584	0.483	142.676	7.3004	DUR12
1997-Mar-07	20:47:01.536	2:26:37.248	23.66	1.5993	0.7078	142.513	14.3409	PRA98
2001-Jun-24	20:37:55.402	0:35:59.309	41.33	1.295	0.4229	305.437	18.6822	DUR12
2002-Feb-16	17:31:59.002	2:59:19.536	11.69	1.5136	0.543	142.021	10.7815	DUR12
2006-Jun-28	20:10:09.696	3:48:58.176	42.34	1.2695	0.3884	309.085	17.2568	DUR12
2006-Jun-29	21:39:57.946	0:02:10.032	42.35	1.2637	0.3781	309.779	16.9759	DUR12
2006-Jun-30	21:08:41.683	0:00:57.802	42.36	1.2583	0.3686	310.427	16.704	DUR12
2006-Jul-25	21:54:52.531	3:58:06.038	46.2	1.1218	0.1632	332.464	0.7458	DUR12
2006-Jul-25	22:22:34.608	3:21:52.733	46.21	1.1217	0.163	332.487	0.7206	DUR12
2007-Feb-10	04:23:01.824	0:17:19.248	9.43	1.4856	0.5093	143.445	9.2355	DUR12
2007-Feb-12	04:50:24.893	8:31:49.411	9.6	1.4952	0.5192	143.284	9.8281	DUR12
2007-Feb-17	03:24:04.867	8:03:41.501	11.6	1.5184	0.5477	142.973	11.1469	DUR12
2007-Feb-17	08:11:48.106	2:46:47.914	11.71	1.5194	0.549	142.963	11.195	DUR12
2007-Feb-18	19:59:42.432	2:33:38.880	12.59	1.5262	0.5588	142.904	11.5563	DUR12
2009-Mar-21	21:50:27.110	2:47:46.723	24.16	1.9018	1.1131	210.032	28.0154	DUR12
2009-Mar-28	20:46:23.434	2:24:54.432	22.61	1.9026	1.0768	210.217	28.9456	DUR12
2009-Apr-15	18:29:56.429	0:44:48.682	20.28	1.8983	1.0229	209.708	30.5989	DUR12
2009-May-17	19:20:18.269	0:55:09.898	25.64	1.8673	1.0752	208.826	30.0859	DUR12
2009-May-18	17:34:34.522	3:12:02.966	25.89	1.866	1.0791	208.863	30.0127	DUR12
2009-May-24	17:54:09.043	9:46:08.717	27.48	1.8567	1.1072	209.226	29.4834	DUR12
2011-May-31	21:30:36.346	0:26:52.742	42.35	1.4105	0.6883	294.664	20.7791	DUR12
2011-Jun-03	22:52:19.200	0:44:40.560	42.57	1.3948	0.6545	296.31	20.5043	DUR12
2011-Jun-03	23:53:48.480	1:31:11.194	42.57	1.3946	0.654	296.334	20.5003	DUR12
2011-Jun-04	21:26:44.275	0:07:24.528	42.64	1.3899	0.6442	296.823	20.412	DUR12
2011-Jun-04	22:52:47.971	0:38:47.443	42.64	1.3896	0.6435	296.856	20.4061	DUR12
2011-Jun-05	21:46:59.232	3:08:55.565	42.71	1.3846	0.6331	297.38	20.3082	DUR12
2011-Jun-05	22:43:32.678	0:40:05.462	42.71	1.3844	0.6326	297.402	20.3042	DUR12
2011-Jun-08	21:34:43.795	0:36:51.235	42.92	1.3689	0.6006	299.045	19.9744	DUR12
2011-Jun-09	21:18:03.283	0:29:00.701	42.99	1.3637	0.59	299.604	19.8543	DUR12
2011-Jun-10	21:26:35.894	3:12:57.571	43.06	1.3584	0.5792	300.177	19.7269	DUR12
2011-Jun-24	22:00:21.110	1:03:30.931	44.05	1.2828	0.4345	308.779	17.2486	DUR12
2011-Jun-26	22:02:13.776	0:16:33.600	44.21	1.2719	0.4147	310.127	16.7548	DUR12
2011-Jun-27	22:07:33.110	0:58:19.891	44.29	1.2664	0.4049	310.817	16.4897	DUR12
2011-Jul-02	04:34:20.669	9:10:07.997	44.67	1.2429	0.364	313.871	15.2133	DUR12
2011-Jul-07	20:50:11.530	1:54:38.304	45.33	1.2117	0.3122	318.31	13.0347	DUR12
2011-Jul-12	19:42:51.898	0:04:48.317	46.2	1.1845	0.2698	322.632	10.5143	DUR12
2011-Jul-22	19:46:34.378	3:22:37.315	50.33	1.1304	0.1969	333.161	2.4984	DUR12
2011-Jul-22	22:17:38.083	2:36:15.149	50.41	1.1298	0.1963	333.288	2.3847	DUR12
2011-Jul-22	23:12:22.579	1:42:24.941	50.44	1.1296	0.196	333.334	2.3436	DUR12
2011-Jul-24	21:18:31.450	0:54:38.362	51.96	1.1194	0.185	335.693	0.1338	DUR12
2011-Jul-26	21:23:41.453	0:48:16.301	53.92	1.1088	0.175	338.268	− 2.4533	DUR12
2011-Jul-27	05:39:39.082	0:36:12.730	54.29	1.107	0.1733	338.715	− 2.9253	DUR12
2011-Aug-13	06:51:40.464	0:15:29.261	81.93	1.023	0.1704	1.786	− 31.6103	DUR12
2011-Aug-14	06:41:30.221	0:14:37.939	83.28	1.0185	0.1745	3.0365	− 33.0291	DUR12
2011-Oct-25	06:40:55.056	8:45:26.842	76.62	0.9527	0.581	100.483	− 34.5387	DUR12
2011-Oct-26	06:45:58.579	8:42:16.502	76.21	0.956	0.5839	101.508	− 34.0919	DUR12
2011-Oct-27	06:43:30.317	8:48:34.070	75.79	0.9593	0.5866	102.514	− 33.6468	DUR12

Table A2 – *continued*

| Date	UT (start)	UT (end)	α[°]	r [au]	Δ [au]	PABLon [°]	PABLat [°]	Reference
2011-Oct-29	06:36:12.787	8:46:36.566	74.97	0.9662	0.5916	104.486	− 32.7562	DUR12
2011-Oct-30	06:39:26.582	8:06:33.437	74.56	0.9698	0.5939	105.457	− 32.3085	DUR12
2011-Nov-01	06:48:30.384	8:38:00.413	73.74	0.9772	0.5982	107.361	− 31.4125	DUR12
2011-Nov-02	06:39:03.427	8:42:33.350	73.34	0.981	0.6001	108.286	− 30.9691	DUR12
2011-Nov-03	06:13:04.598	8:41:28.464	72.94	0.9849	0.6019	109.188	− 30.5313	DUR12
2011-Dec-09	01:01:18.221	3:28:25.363	58.16	1.1592	0.5874	134.694	− 15.2567	DUR12
2011-Dec-29	21:15:27.331	2:57:07.891	46.15	1.2735	0.5303	143.199	− 6.737	DUR12
2012-Jan-30	03:06:49.363	1:10:11.165	17.79	1.4384	0.488	146.03	5.9592	DUR12
2014-Apr-20	04:22:33.571	1:36:08.006	20.39	1.894	1.0179	210.571	30.8605	WAR17
2014-Apr-21	06:32:02.141	1:57:18.259	20.43	1.8933	1.0172	210.51	30.9005	WAR17
2014-Apr-23	03:57:00.749	1:53:01.133	20.53	1.8919	1.0164	210.405	30.9576	WAR17
2016-May-31	08:13:12.518	1:24:47.261	43.56	1.3971	0.6938	296.851	19.899	WAR17
2016-Jun-01	08:14:37.709	1:11:25.296	43.66	1.3919	0.6827	297.42	19.7959	WAR17
2016-Jun-02	08:07:52.234	0:56:13.085	43.77	1.3867	0.6717	297.99	19.6891	WAR17
2016-Jun-03	08:05:50.669	1:20:24.691	43.88	1.3815	0.6607	298.566	19.5775	WAR17
2016-Jun-04	08:04:31.786	1:16:02.122	43.99	1.3763	0.6498	299.147	19.4612	WAR17
2017-Feb-05	19:31:47.136	0:55:15.658	13.65	1.4864	0.5228	147.534	9.2321	DUR18
2017-Feb-15	23:59:19.046	4:56:09.024	11.36	1.534	0.5633	146.666	12.1105	DUR18

Table A3. Archival observations for (12711) Tukmit. The information includes the date, the starting and end time (UT) of the observations, the phase angle (α), the heliocentric (r), and geocentric (Δ) distances, phase angle bisector longitude (PABLon) and latitude (PABLat) of the asteroid at the time of observation. **References:** WS22: Warner & Stephens (2022).

| Date	UT (start)	UT (end)	α[°]	r [au]	Δ [au]	PABLon [°]	PABLat [°]	Reference
2021-Nov-29	08:24:37.325	3:18:03.658	39.6	1.4849	0.8661	118.675	17.9726	WS22
2021-Nov-30	08:25:33.830	3:27:22.234	39.42	1.4836	0.8541	118.936	17.6979	WS22

Table A4. Archival observations for (161989) Cacus. The information includes the date, the starting and end time (UT) of the observations, the phase angle (α), the heliocentric (r) and geocentric (Δ) distances, phase angle bisector longitude (PABLon) and latitude (PABLat) of the asteroid at the time of observation. **References:** SCH79: Schuster, Surdej & Surdej (1979); DEG78: Degewij, Lebofsky & Lebofsky (1978); KOE14: Koehn et al. (2014); DUR18: Ďurech et al. (2018).

| Date	UT (start)	UT (end)	α[°]	r [au]	Δ [au]	PABLon [°]	PABLat [°]	Reference
1978-Mar-01	02:10:20.064	8:04:20.554	8.44	1.1316	0.1425	156.682	− 3.9248	SCH79
1978-Mar-08	03:58:30.691	9:03:15.091	25.62	1.1069	0.1284	153.717	8.1938	DEG78
2003-Feb-18	00:32:52.253	6:25:12.432	28.51	1.1863	0.2325	146.066	− 20.5229	DUR18
2003-Mar-05	18:11:19.622	9:08:36.701	35.15	1.1341	0.1807	141.547	− 4.6256	DUR18
2003-Mar-25	18:49:27.408	3:21:20.160	67.17	1.0636	0.2294	143.1	21.3483	DUR18
2003-Apr-01	19:15:52.243	0:08:22.301	74.1	1.0388	0.2618	146.707	28.8395	DUR18
2003-Apr-04	20:01:34.234	0:58:15.715	76.45	1.0282	0.2763	148.628	31.8365	DUR18
2009-Feb-19	09:04:52.550	2:29:30.422	50.96	1.1211	0.2379	186.977	0.3458	KOE14
2014-Dec-21	05:34:44.371	8:31:08.112	51.19	1.2536	0.9041	159.459	− 17.1859	DUR18
2015-Feb-17	06:55:48.605	9:04:36.307	67.61	1.0667	0.4663	207.04	11.6119	DUR18
2015-Feb-17	08:16:10.675	8:31:27.379	67.63	1.0665	0.4661	207.097	11.6582	DUR18
2015-Oct-09	07:26:34.714	8:55:20.410	50.18	1.3003	0.8079	72.094	− 35.7728	DUR18
2015-Oct-13	07:30:26.179	9:07:28.762	49.64	1.3081	0.7994	74.1272	− 36.8006	DUR18
2015-Nov-05	05:58:17.011	8:49:43.018	46.57	1.3433	0.7449	84.312	− 41.7277	DUR18
2015-Dec-08	05:14:32.352	8:38:07.757	42.53	1.3632	0.6561	93.524	− 45.3206	DUR18
2015-Dec-15	04:48:22.032	8:25:47.741	41.86	1.3627	0.6381	94.5876	− 45.3522	DUR18
2016-Feb-04	03:24:48.499	5:03:14.803	44.61	1.3093	0.5769	100.413	− 33.8912	DUR18
2016-Feb-12	00:23:39.811	1:57:33.005	46.51	1.2936	0.5847	102.37	− 30.374	DUR18
2016-Mar-09	23:53:28.608	3:32:30.739	53.87	1.2258	0.6441	112.676	− 16.8207	DUR18
2016-Oct-05	23:43:01.776	3:23:46.378	66.03	1.0888	0.3437	323.976	− 17.9056	DUR18
2016-Dec-22	00:37:07.046	3:09:58.061	48.43	1.3102	0.9512	23.6428	− 32.6566	DUR18
2016-Dec-31	01:00:04.435	3:47:11.587	47.42	1.3258	1.015	29.5956	− 32.4289	DUR18

APPENDIX B: STATISTICAL QUALITY OF POLE SOLUTIONS
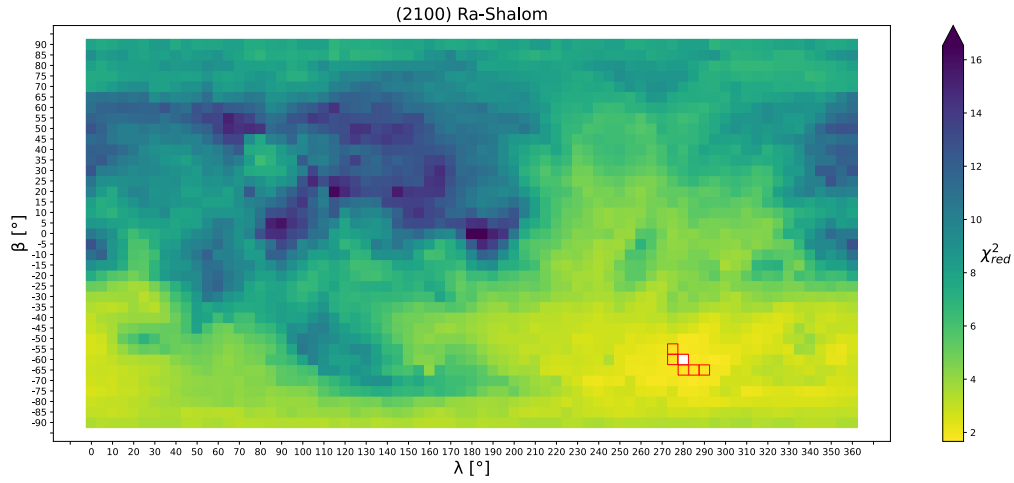
Figure B1. Statistical quality of (2100) Ra-Shalom pole solutions obtained with the constant period code. The solutions are shaded by its χ^2_{red} value. The best solution obtained is shown as a white square ($\lambda = 278°$, $\beta = -60°$) with $\chi^2_{red} = 1.66$ (normalized by the 4987 data points). The solutions within a margin of 5.7 per cent (3σ) are highlighted with a red border.
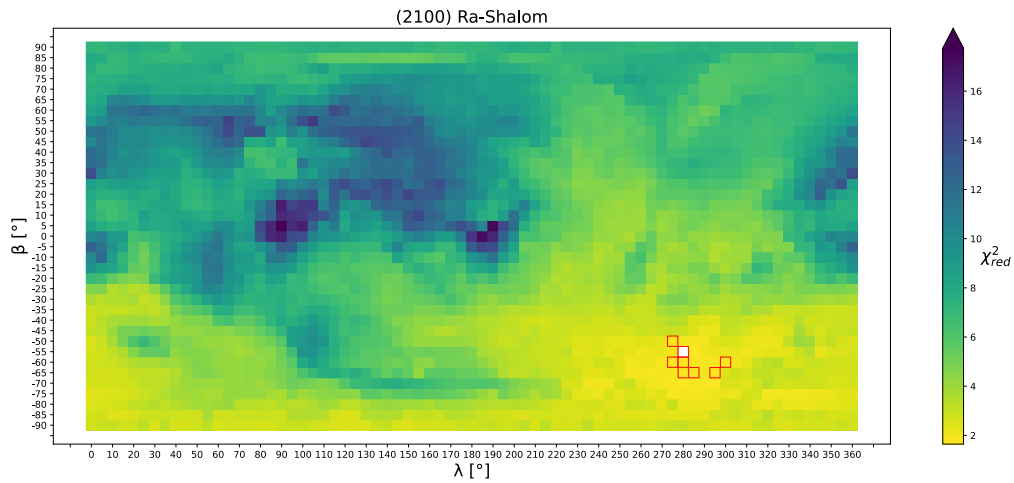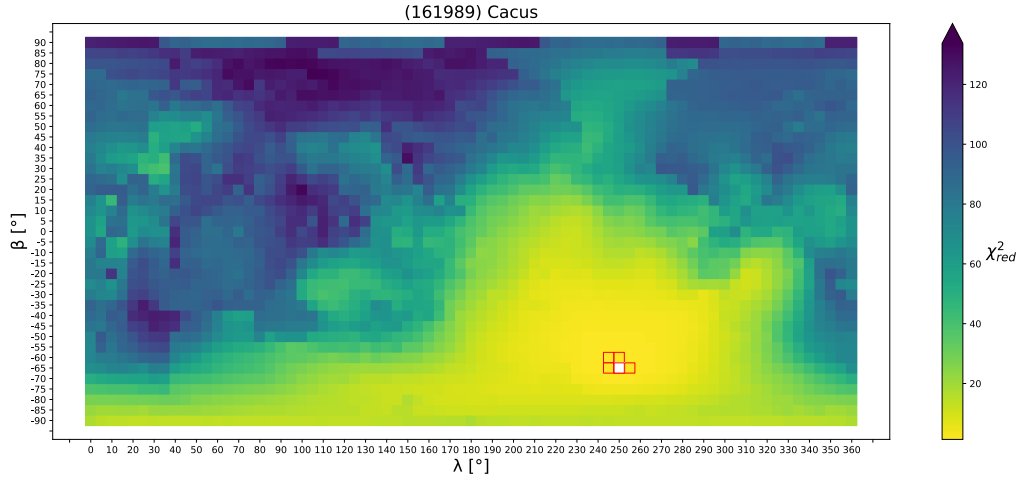

Figure B2. Statistical quality of (2100) Ra-Shalom pole solutions obtained with the linear increasing period code. The solutions are shaded by its χ^2_{red} value. The best solution obtained is shown as a white square ($\lambda = 283°$, $\beta = -62°$) with $\chi^2_{red} = 1.64$ (normalized by the 4987 data points). The solutions within a margin of 5.7 per cent (3σ) are highlighted with a red border.
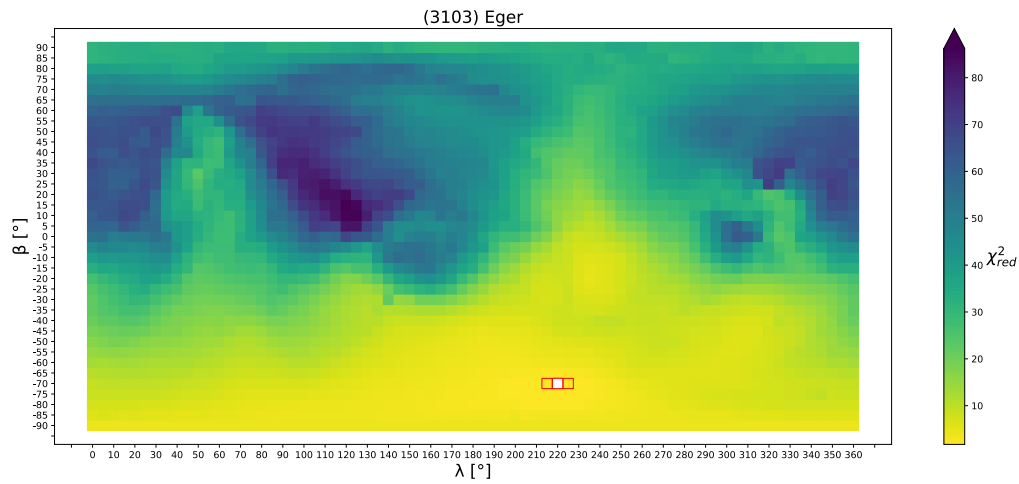
Figure B3. Statistical quality of (3103) Eger pole solutions obtained with the linear increasing period code. The solutions are shaded by its χ^2_{red} value. The best solution obtained is shown as a white square ($\lambda = 214°$, $\beta = -71°$) with a $\chi^2_{\mathrm{red}} = 1.74$ (normalized by the 6034 data points), the solutions within a margin of 5.2 per cent (3σ) are highlighted with a red border.
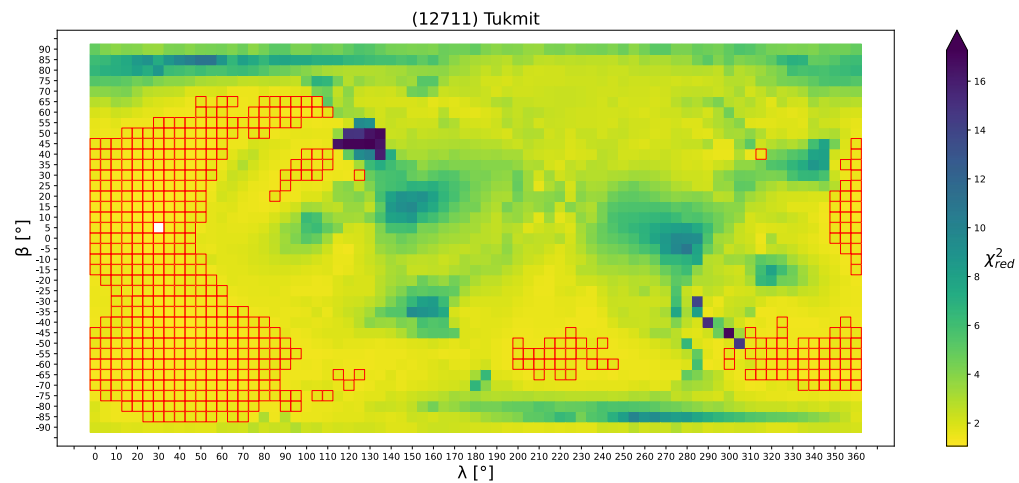

Figure B4. Statistical quality of (12711) Tukmit pole solutions obtained with the constant period code. The solutions are shaded by its χ^2_{red} value. The best solution obtained is shown as a white square ($\lambda = 27°$, $\beta = 11°$) with a $\chi^2_{\mathrm{red}} = 1.06$ (normalized by the 263 data points), the solutions within a margin of 25 per cent (3σ) are highlighted with a red border.

Figure B5. Statistical quality of (161989) Cacus pole solutions obtained with the linear increasing period code. The solutions are shaded by its $\chi^2_{\rm red}$ value. The best solution obtained is shown as a white square ($\lambda = 251°$, $\beta = -61°$) with a $\chi^2_{\rm red} = 1.31$ (normalized by the 1534 data points), the solutions within a margin of 10 per cent (3σ) are highlighted with a red border.
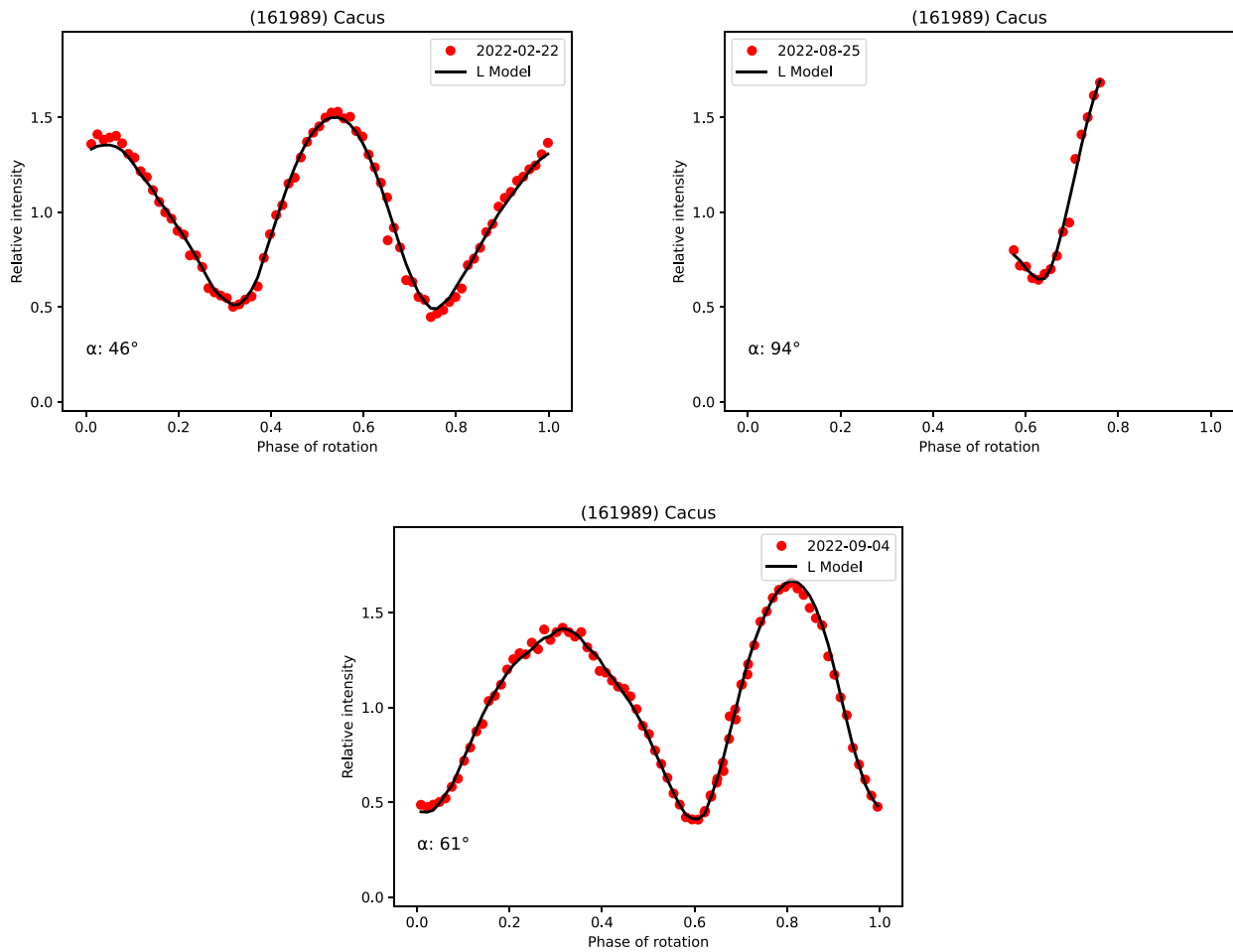
APPENDIX C: FITS OF MODELS AND DATA
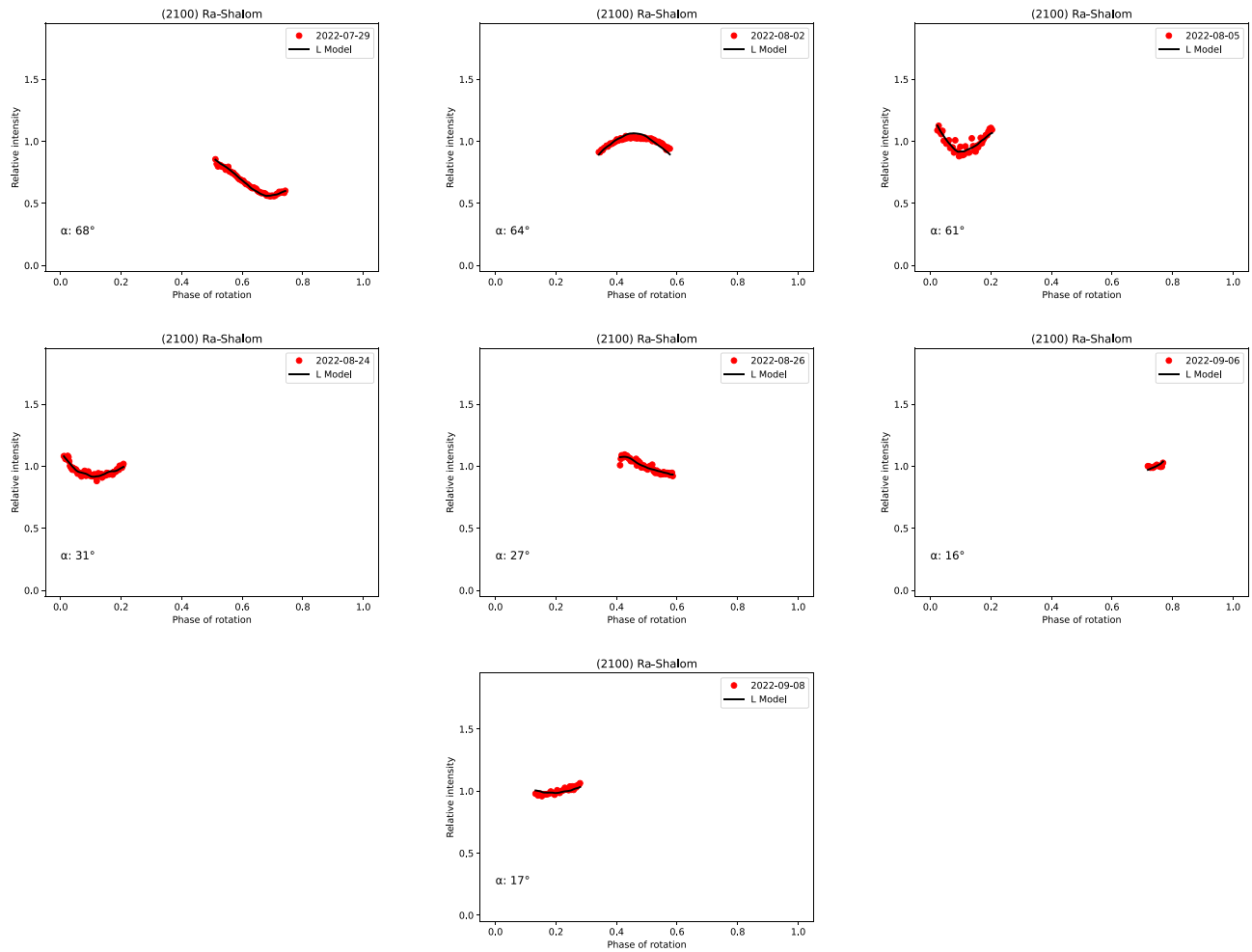
Figure C1. Fit between light curves from (2100) Ra-Shalom presented in this paper and the best-fitting linearly increasing period model (L Model). The data is plotted as dots for each observation, meanwhile the model is plotted as a solid black line. The geometry is described its solar phase angle α.
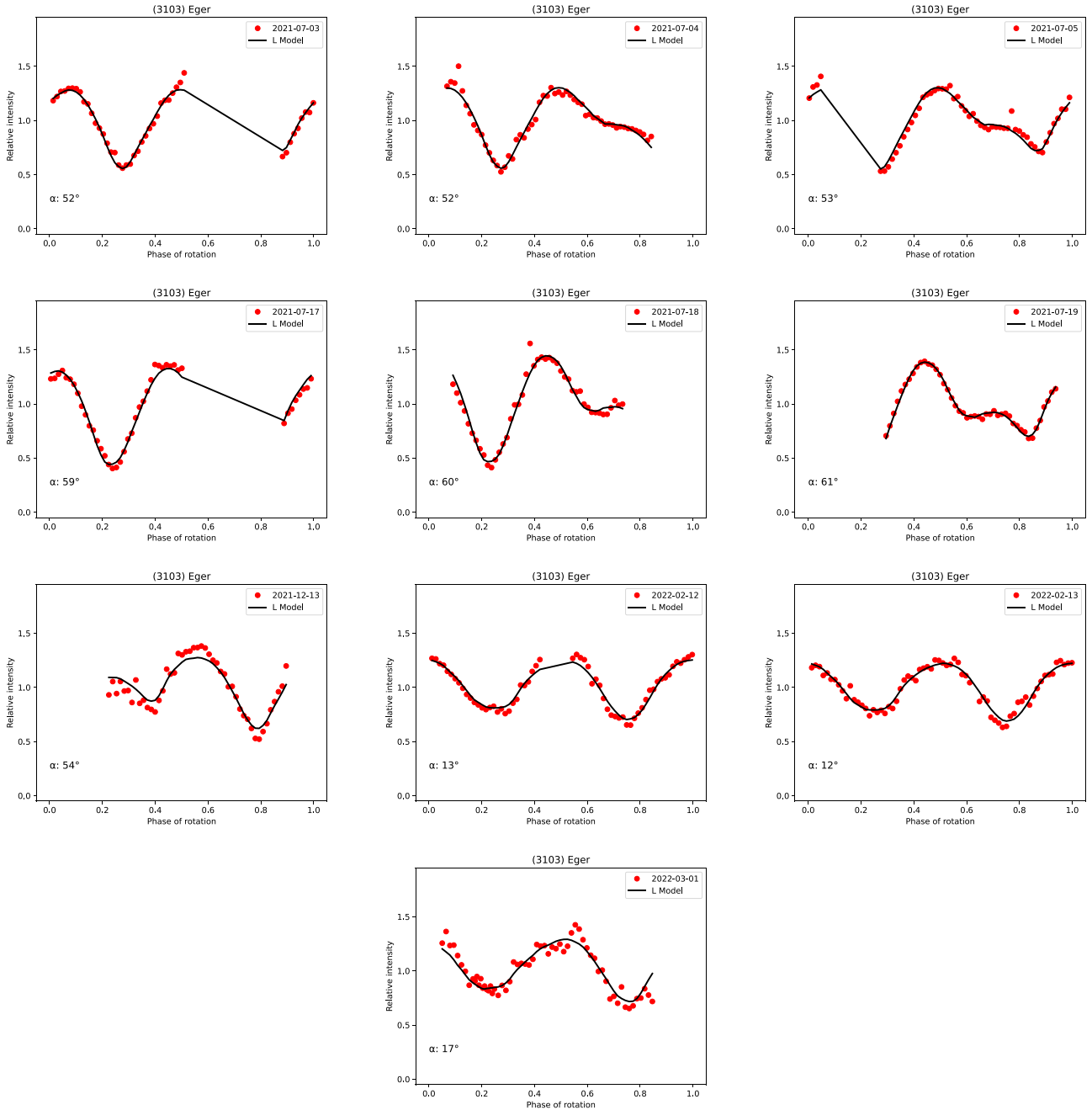
Figure C2. Fit between light curves from (3103) Eger presented in this paper and the best-fitting linearly increasing period model (L Model). The data is plotted as red dots for each observation, meanwhile the model is plotted as a solid black line. The geometry is described its solar phase angle α.

Figure C3. Fit between light curves from (161989) Cacus presented in this paper and the best-fitting linearly increasing period model (L Model). The data is plotted as red dots for each observation, meanwhile the model is plotted as a solid black line. The geometry is described its solar phase angle α.

This paper has been typeset from a TEX/LATEX file prepared by the author.